Key features of the IPSL ocean atmosphere model and its sensitivity to atmospheric resolution

Olivier Marti · P. Braconnot · J.-L. Dufresne · J. Bellier · R. Benshila · S. Bony · P. Brockmann · P. Cadule · A. Caubel · F. Codron · N. de Noblet · S. Denvil · L. Fairhead · T. Fichefet · M.-A. Foujols · P. Friedlingstein · H. Goosse · J.-Y. Grandpeix · E. Guilyardi · F. Hourdin · A. Idelkadi · M. Kageyama · G. Krinner · C. Lévy · G. Madec · J. Mignot · I. Musat · D. Swingedouw · C. Talandier

Abstract This paper presents the major characteristics of the Institut Pierre Simon Laplace (IPSL) coupled ocean–atmosphere general circulation model. The model components and the coupling methodology are described, as well as the main characteristics of the climatology and interannual variability. The model results of the standard version used for IPCC climate projections, and for intercomparison projects like the Paleoclimate Modeling Intercomparison Project (PMIP 2) are compared to those with a higher resolution in the atmosphere. A focus on the North Atlantic and on the tropics is used to address the impact of the atmosphere resolution on processes and feedbacks. In the North Atlantic, the resolution change leads to an improved representation of the storm-tracks and the North Atlantic oscillation. The better representation of the wind structure increases the northward salt transports, the deep-water formation and the Atlantic meridional overturning circulation. In the tropics, the ocean–atmosphere dynamical coupling, or Bjerknes feedback, improves with the resolution. The amplitude of ENSO (El Niño-Southern oscillation) consequently increases, as the damping processes are left unchanged.

Keywords Climate · Simulations · Ocean · Atmosphere · Coupling · Circulation · El Niño/Southern oscillation · North-Atlantic oscillation · Storm-tracks · Resolution · Coupling

O. Marti (✉) · P. Braconnot · J. Bellier · P. Brockmann ·
A. Caubel · N. de Noblet · P. Friedlingstein · A. Idelkadi ·
M. Kageyama
IPSL/LSCE, unité mixte CEA-CNRS-UVSQ, Bât 712,
Orme-des-Merisiers, 91191 Gif-sur-Yvette Cedex, France
e-mail: olivier.marti@lsce.ipsl.fr

J.-L. Dufresne · S. Bony · F. Codron · L. Fairhead ·
J.-Y. Grandpeix · F. Hourdin · I. Musat
IPSL/LMD, Unité mixte CNRS-Ecole Polytechnique-ENS-
UPCM, Case 99, 4 Place Jussieu, 75252 Paris Cedex 05, France

D. Swingedouw
CNRS/CERFACS, 42 Avenue Gaspard Coriolis,
31057 Toulouse, France

T. Fichefet · H. Goosse
Institut d'Astronomie et de Géophysique Georges Lemaître,
Université Catholique de Louvain, Chemin du Cyclotron,
2, 1348 Louvain-la-Neuve, Belgium

R. Benshila · E. Guilyardi · C. Lévy · G. Madec · J. Mignot ·
C. Talandier
IPLS/LOCEAN, unité mixte CNRS-IRD-UPMC, Case 100,
4 Place Jussieu, 75252 Paris Cedex 05, France

P. Cadule · S. Denvil · M.-A. Foujols
Institut Pierre Simon Laplace des Sciences de l'Environnement
(IPSL), 4 Place Jussieu, 75252 Paris Cedex 05, France

G. Krinner
LGGE, Unité mixte CNRS-UJF Grenoble, BP96,
38402 Saint-Martin-d'Hères, France

1 Introduction

Climate is the result of complex interactions between several subsystems. To understand how climate evolves depending on external forcing, climate system models are becoming more and more complex. Starting from atmosphere only models in the 1960s', climate models incorporate now components of ocean, sea ice, land, vegetation, and possibly the carbon cycle, the atmospheric chemistry, atmospheric aerosols or oceanic tracers. These powerful tools are commonly used for future climate projections (IPCC 2007, Fig. 4b).

The IPSL CM4 model (Marti et al. 2005) couples four components of the Earth system: LMDZ (Hourdin et al. 2006) for atmospheric dynamics and physics, OPA (Madec

et al. 1997) for ocean dynamics, LIM (Fichefet and Morales-Maqueda 1997; 1999) for sea ice dynamics and thermodynamics, and ORCHIDEE (Krinner et al. 2005) for the land surface. Successive versions of the global coupled model have been developed since 1995. Since the first version of the coupled model, our goal was to design and develop a global coupled model with no flux correction at the air–sea interface that can be used to study present, future and past climates. Substantial development and analysis concerned the conservation of energy and water, so that comprehensive analyses of heat and water budget and transport are possible.

The first version of the model (Braconnot et al. 1997) was built with the LMD 5.3 version of the LMD atmospheric model, the OPA 7 version of the ocean model developed at LODYC, and a simple sea ice component. The first coupled simulations (Braconnot et al. 1997) exhibited a large drift in surface air temperature, which has been attributed to an energetic imbalance of the atmospheric model. Several adjustments were performed. A first set of modifications has improved the atmosphere boundary layer over mixed sea ice and ocean grid cells. A second set was designed to equilibrate the atmospheric model, by adjusting the threshold for vertical diffusion in stable cases, which allowed for better simulation of temperature inversions at high latitudes (Krinner et al. 1997). Other adjustments concern the drag coefficient in stable cases and the balance between long wave and short wave radiation at the top of the atmosphere (reduction of the water droplet size from 15 to 8 µm). Although these adjustments allow stable coupled simulations, the energy absorbed in the tropical region was underestimated, which explains the cold tropical bias in the tropics (Braconnot et al. 2000). Mid-latitude experienced a reversed bias. These characteristics improved with a new version of the Morcrette et al. (1986) radiative scheme. The hydrological cycle was also closed in this revised version, thanks to a simple routing scheme that considered the 46 major rivers (Le Clainche 1996). Following the work of Guilyardi et al. (2001), isopycnal diffusion was implemented in the ocean model. A revised version of the interpolation scheme (Marti et al. 2005) also contributed to the local and global conservation of energy at the air–sea interface.

The next step of the model development consisted in implementing the complex IPSL thermodynamic sea ice model (L'Heveder 1999; Filiberti et al. 2001). This required some adjustment in the coupling procedure. In particular, in this IPSL CM2 version, the sea ice model computed sea ice albedo, and other surface parameters (Braconnot et al. 2000). The derivative of the fluxes with respect to temperature was also provided to the sea ice model to insure the stability of the coupling over sea ice, following the detailed stability analysis of Dufresne and Grandpeix (1996). This version of the model yields to interesting results about the analyses of the response of the climate to changes in insolation (Braconnot and Marti 2003; Khodri et al. 2005). It was also coupled to a carbon cycle model, to perform the first climate simulations (present and future) with an interactive carbon cycle (Friedlingstein et al. 2001; Dufresne et al. 2002). However, some biases in the model climatology needed to be corrected. Increased interest for mid and high latitudes climate leads also to the need for a better resolution at high latitudes. Due to the cold bias of the model in the tropics, several aspects of the tropical interannual variability, such as the representation of ENSO (El Niño-Southern Oscillation), needed improvement.

The latest developments lead to a completely new model used for CMIP3 (Meehl et al. 2007), the multimodel ensembles climate projections used in the intergovernmental panel on climate change (IPCC) assessment report AR4 (IPCC 2007). The model climatology and the representation of the interannual variability were greatly improved compared to the previous generations, even though some biases are still present. The objective of this paper is to present the major characteristics of the IPCC AR4 version of the coupled model (Dufresne et al. 2005) and of its climatology. The results of the reference version are now in several databases (and PMIP II Braconnot et al. 2007a, b; CMIP, Meehl et al. 2007), and used in several scientific works. This papers aims to help the database users by explaining the main characteristics of the simulated climate, and the origin of the model biases. Several aspects of model climatology and variability are affected by the resolution. From the reference version at medium resolution, we discuss the impact of the atmospheric resolution on the key climatic features in the tropics and the mid-latitude.

Section 2 of the paper presents the model components and the methodology of the coupling. Section 3 presents the experiments, their global energetics, and the main characteristics of the surface climate. Section 4 focuses on two regions, Atlantic and tropics, and discusses the mechanisms yielding to differences between the two resolutions. Conclusion is given in Section 5.

2 The model

2.1 Model components

2.1.1 The atmospheric model LMDZ

The atmospheric component of the IPSL CM4 model, LMDZ (Hourdin et al. 2006), is a state-of-the-art atmospheric general circulation model, inherited from the

original climate model of Laboratoire de Météorologie Dynamique of Sadourny and Laval (1984).

The dynamical part of the code is based on a finite-difference formulation of the primitive equations of meteorology. The discretization insures numerical conservation of both enstrophy for barotropic flows and angular momentum for the axi-symmetric component. Vapor and liquid water are advected with a monotonic second order finite volume scheme (Van Leer 1977; Hourdin et al. 1999). For the current grids the time-step is of 2 h for the radiation scheme, 30 min for physics, and 6 min (standard resolution) or 3 min (high resolution) for the dynamics. For latitudes poleward of 60° in both hemispheres, a longitudinal filter is applied in order to limit the effective resolution to that at 60°.

Coupled to the dynamical core, the model includes a set of physical parameterizations. The radiation scheme is the one introduced several years ago in the model of European Centre for Medium-Range Weather Forecasts (ECMWF) by Morcrette et al. (1986): the solar part is a refined version of the scheme developed by Fouquart and Bonnel (1980) and the thermal infra-red part is due to Morcrette et al. (1986). Condensation is parameterized separately for convective and non-convective clouds. Moist convection is treated using mass flux approaches. During the preparation of the IPSL CM4 model, Emanuel (1991) convection scheme was adopted in place of Tiedtke (1989) scheme. The sensitivity of the simulated climate to the convection scheme has been studied by Hourdin et al. (2006) for the atmosphere alone, and by Braconnot et al. 2007a, b for the ocean–atmosphere model. Clouds are represented through a log-normal probability distribution function of subgrid scale total (vapor and condensed) water (Le Treut and Li 1991; Bony and Emanuel 2001). Effects of mountains (drag, lifting, gravity waves) are accounted for using a state-of-the-art scheme (Lott 1997, 1999).

For coupling purposes, a fractional land–sea mask was introduced in the model. Each grid box was then divided into four sub-surfaces corresponding to land surface, free ocean, sea ice and glaciers. Surface fluxes are computed using parameters (roughness length, albedo, temperature, humidity, etc.) adapted to each surface type. For each atmospheric column, vertical diffusion is applied independently for each sub-surface, and the resulting tendencies are averaged. In addition an interface model was also introduced to disconnect more easily surface processes from the atmosphere (see Sect. 2.2). The diffusion scheme was rewritten to systematically force the boundary layer by surface fluxes. The computation of surface fluxes is done in an independent model that requires providing this model with the sensitivity of the turbulent flux to temperature, in order to preserve the properties of the semi-implicit scheme. With this formulation the flux model can be either

a routine in the atmospheric model, an ocean model or a land surface scheme.

2.1.2 The land surface model ORCHIDEE

ORCHIDEE (Krinner et al. 2005) is divided is three modules, devoted respectively to hydrology, carbon cycle and vegetation dynamics. Only the hydrological module SECHIBA (Ducoudré et al. 1993; Verant et al. 2004) is activated here. It has been developed as a set of surface parameterizations for an atmospheric general circulation model. It describes the short-timescale processes (of the order of a few minutes to hours) of energy and water exchanges between the atmosphere and the biosphere. The parameterizations of photosynthesis follow Farquhar et al. (1980) for C_3 plants and Collatz et al. (1992) for C_4 plants. Stomatal conductance is calculated following Ball et al. (1987), including the dependence on CO_2 concentration. The other two modules have not been activated in this study.

ORCHIDEE includes (in SECHIBA) a routing scheme which combines the horizontal flow of water in the river basins with the vertical processes classically included in land surface models. It is based on the work of Hagemann and Dümenil (1998), and uses a cascade of three reservoirs: the stream and two aquifer reservoirs, each being associated with only one time constant. In each grid-cell the runoff and drainage are the water supply of the routing system. ORCHIDEE in this configuration has been validated over a wide range of regions and time scales and gives satisfactory results as discussed in Verant et al. (2004) and Ngo-Duc et al. (2005). The description of land ice included in ORCHIDEE is not used when coupled to the atmosphere.

2.1.3 The oceanic component: the OPA system

The OPA system (Andrich 1988; Madec et al. 1997) is a primitive equation model of both the regional and global ocean circulation. The OPA reference manual (Madec et al. 1997) details the ocean physics as taken into account by the model (explicitly or using sub-grid parameterization) as well as boundary conditions (surface, bottom, lateral), numerical schemes and computer implementation (http://www.lodyc.jussieu.fr/opa).

The ocean configuration used here is named ORCA2. Its specificity lies on the horizontal curvilinear mesh used to overcome the North Pole singularity found for geographical meshes. The common geographical coordinate system has a singular point at the North Pole that cannot be easily treated in a global model without filtering. A solution consists in the use of a tripolar grid (Madec and Imbard 1996; Murray 1996). The grid is based on a 2° Mercator

mesh (i.e., variation of meridian scale factor as cosinus of the latitude). In the northern hemisphere the mesh has two poles, over Canada and Siberia. The ratio of anisotropy is nearly one everywhere. The mean grid spacing is about 2/3°. The latitudinal resolution is refined to 1° near the equator, and in the Mediterranean Sea. The Gibraltar Strait is explicitly resolved, with a width of 111 km. The vertical domain spreads from the surface to a depth of 5,000 m. There are 31 levels, with 10 levels in the top 100 m.

The eddy viscosity coefficient on momentum depends on the geographical position. It is taken as 40,000 m^2 s^{-1}, reduced to 2,000 m^2 s^{-1} in the equator regions except near the western boundaries. Diffusion on tracer acts along the isopycnal surfaces (neutral surfaces) with an eddy diffusivity coefficient of 2,000 m^2 s^{-1}. The eddy induced velocity parametrization uses a coefficient that depends on the growth rate of baroclinic instabilities (it usually varies from 15 to 3,000 m^2 s^{-1}). The Beckman (1998) diffusive bottom boundary layer parameterization is applied along continental slopes. A linear friction is applied on momentum. To parameterize ocean convection, the vertical eddy viscosity and diffusivity coefficients are increased to 100 m^2 s^{-1} in case of static instability. The free surface formulation of Roullet and Madec (2000) is used.

2.1.4 The LIM sea ice model

LIM (Louvain-la-Neuve sea Ice Model) is a thermodynamic–dynamic sea ice model specifically designed for climate studies (Fichefet and Morales-Maqueda 1997, 1999). Sensible heat storage and vertical heat conduction within snow and ice are determined by a three-layer model (one layer for snow and two layers for ice). The effect of the subgrid scale snow and ice thickness distributions is accounted for through an effective thermal conductivity, which is computed by assuming that the snow and ice thicknesses are uniformly distributed between zero and twice their mean value over the ice-covered portion of the grid cell. The storage of latent heat inside the ice resulting from the trapping of shortwave radiation by brine pockets is taken into account. The surface albedo is parameterized as a function of the surface temperature and the snow and ice thicknesses. The model allows for the presence of leads within the ice pack. Vertical and lateral growth and decay rates of the ice are obtained from prognostic energy budgets at both the bottom and surface boundaries of the snow–ice cover and in leads. Snow aging is parameterized identically in LIM, ORCHIDEE and LMDZ. The viscous-plastic constitutive law proposed by Hibler (1979) is used for computing the internal ice force. The ice strength is taken as a function of the ice thickness and compactness. The sea ice model runs on the same grid as OPA.

2.2 The coupled model

#### 2.2.1 Coupling between atmosphere and surface

The coupling scheme of the previous versions of the IPSL model (Braconnot et al. 2000; Dufresne et al. 2002) has been revisited to ensure both global and local conservations of momentum, heat and fresh water fluxes at the air–sea interface. Following some of the ideas implemented in previous model versions (Dufresne and Grandpeix 1996; Braconnot 1998), an interface model was implemented in the atmospheric model. Each atmospheric column is interfaced with up to four different surface types: ocean, land, sea ice and land ice. Turbulent surface fluxes and surface temperature are computed separately on each sub-surface, according to the surface characteristics (roughness length, stability, etc.). The fluxes are sent to each sub-model (ocean, sea ice, land, glacier). In the atmosphere, the flux is the weighted sum of the fluxes computed for each subsurface. The computation of turbulent fluxes is detailed in the appendices. The radiative fluxes are computed in the atmospheric column, and redistributed on each subsurface taking into account the local properties of each subsurface (i.e. the albedo for the short wave flux, and temperature for the long wave flux). The redistribution is conservative. The coupling sequence yields a small loss or gain in energy and water. The LMDZ model computes average surface fluxes over free ocean and over sea ice during the coupling time-step $t - 1$ (currently 1 day). These fluxes are then sent to ORCA that uses them with a sea ice cover that has evolved, and keeps evolving during the time-step t. At the end of time-step t, the integrated flux received by the ocean could thus be slightly different from those sent at the end of time-step $t - 1$.

2.2.2 Atmosphere/ocean/sea ice coupling

Figure 1 shows the fields exchanged between ocean, atmosphere and sea ice. For most of the fields, the sea ice model acts as an interface model between atmosphere and ocean. The sea ice model receives the fluxes for free ocean and sea ice. It computes the evolution of sea ice, and computes the fluxes at the interface between the sea–ice and the ocean. The ocean receives only average fluxes and does not know the fraction of sea–ice. The ocean–sea ice interaction is exactly the same when the ocean–ice model is forced by climatology (e.g. see Timmermann et al. 2004) or coupled to an atmosphere model.

Amongst the fields sent by the atmosphere is $\partial Q/\partial T$. This field is the derivative of turbulent heat fluxes over sea ice with respect to surface temperature. To compute the temperature at the upper surface of the ice, LIM uses an implicit scheme for which the derivative of non-solar

Fig. 1 Fields exchanged between ocean, sea ice and atmosphere models
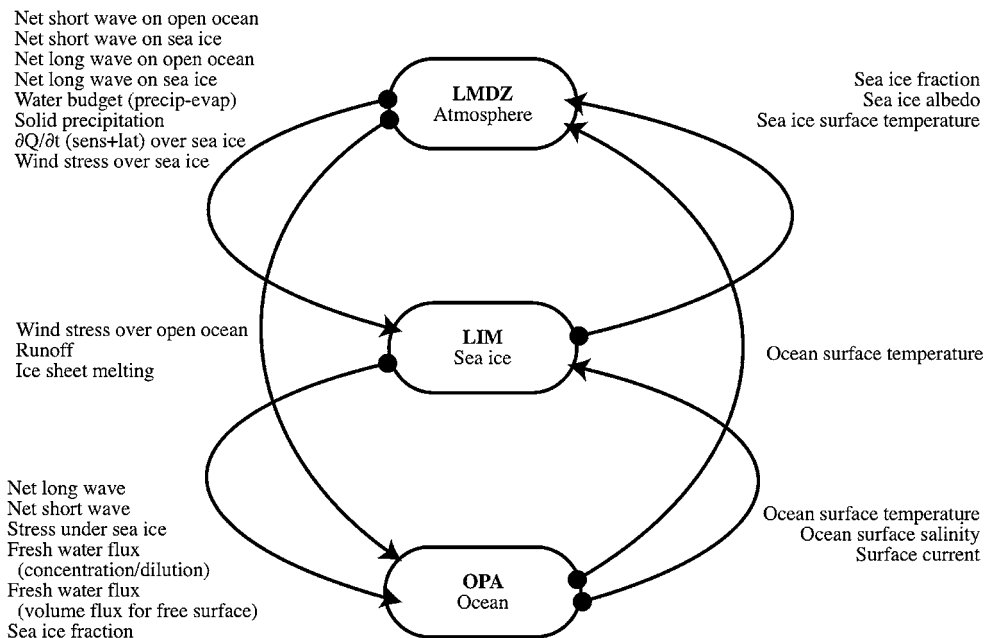
fluxes is needed. LIM computes the derivative of the long wave flux using the black body law, and adds the part from turbulent fluxes computed by LMDZ. The OASIS coupler (Valcke 2006) is used to synchronize the models, and interpolate and exchange fields.

2.2.3 Grids, interpolations and coastline

The atmosphere (LMDZ) and the surface model (ORCHIDEE) run on a regular longitude/latitude grid, whereas the ocean (OPA) and sea ice (LIM) run on a stretched grid. Vector fields (wind stress) are interpolated from atmosphere to ocean with a bicubic scheme. Scalar fields (heat and water fluxes, temperatures, sea ice fractions and albedos, but not calving) are interpolated using a first-order conservative remapping (Jones 1999).

The ocean bathymetry and coastline are derived from the 2-min resolution Etopo2 bathymetry file of NGDC (National Geophysical Data Center), which is a combination of the satellite-based bathymetry (Smith and Sandwell 1997) and IBCAO in the Arctic (Jakobsson et al. 2000). It has been merged with the BEDMAP data (Lythe and Vaughan 2001) beyond 72°S in the Antarctic. In the ocean, a grid box is either fully ocean (mask = 1) of fully land (mask = 0). To keep exactly the same coastline in the ocean and the atmosphere models, the ocean mask is interpolated toward the atmosphere using the method used for scalar fields. This gives the fractions of land and ocean in each atmospheric grid box. In the ocean fraction, repartition between free ocean and sea–ice is given by the sea–ice model at each coupling step. The atmosphere computes the fluxes on each subsurface, allowing an exact

local and global conservation of each quantity, even at the coast.

2.2.4 Closure of the fresh water budget

Snow can accumulate on some grid points, particularly on glaciers. The effect will be a decreased of the sea level. In nature, and if the climate is stable, the dynamics of the ice–sheet should compensate the sea level depletion, through the calving of iceberg. Calving needs to be taken into account in the water budget. On land–ice surface, the local snow mass is limited to 3,000 kg m^{-2}. At each time-step, the snow mass over this limit is sent as calving to the ocean, with a time filtering over 10 years (see Appendix 1.3). A specific interpolation scheme is applied to calving: Earth is divided in three latitude bands with limits at 90°S/50°S/40°N/90°N. In each band, the calving is integrated and evenly sent to the ocean in the same latitude band. As the model is used for paleoclimate studies (Braconnot et al. 1999; Kageyama et al. 1999; Pinot et al. 1999; Kageyama et al. 2001; Alkama et al. 2006), the 40°N limit was chosen because it corresponds to the southernmost latitude reached by icebergs during ice ages (Heinrich events). For the northern band, the calving is sent to the Atlantic and the Arctic, but not to the Pacific. Calving pours directly in the ocean, under sea ice, like river run-off.

In the ocean model several 'seas' are separated from the global ocean (North American Great Lakes, Caspian Sea and Black Sea). The global balance of water is equilibrated in the model. When averaged over the ocean and over several decades, the water flux going into the ocean (net result of precipitation, run-off, calving and evaporation) is

close to zero. This is not true for each individual closed area, which may create a net transfer of water between the global ocean and the closed sea. To avoid any drift of salinity in both closed seas and global ocean, closed seas benefit from a special treatment. The water budget over each individual closed sea is set to zero. The water that should pours into each closed sea (or evaporates from) is added to the water budget of the global ocean, with three different schemes: (1) for the Black Sea, the water budget of the closed sea goes to closest oceanic grid point, mimicking the water flux in the straits; (2) for the North American Great Lakes, if the water budget is positive (excess of water), it goes to the ocean, at the mouth of the St-Lawrence river. If it is negative (evaporation), it is spreaded over the whole open ocean; (3) for the Caspian sea, the water budget, either positive or negative, is spreaded over the whole open ocean.

3 Experiments and main characteristics

3.1 Experiments

Two simulations are presented in the paper, that use the same ocean model and two different atmospheric resolutions. Experiment CTRL is run with a horizontal resolution of the atmosphere of 96 points in longitude and 71 points in latitude ($3.7° \times 2.5°$). This model corresponds to the reference version of the IPSL model used for future climate projection (Dufresne et al. 2005) for the IPCC AR4 report. The HiRes experiment uses a 144×96 atmospheric resolution ($2.5° \times 1.875°$). Both simulations use 19 levels on the vertical, and the same set of model parameters in all submodels, with no change of turbulent viscosity and diffusion. Before coupling, the atmosphere model is equilibrated so that the net heat flux at the top of the atmosphere is close to zero in global and multi-year averages (absolute value less than 0.1 W^{-1} m^{-2}) under modern condition. The tuning only affects the radiative properties of the atmosphere. It concerns parameters such as the droplet size or the subgrid scale distribution of water vapour following Hourdin et al. (2006). Then the model is coupled. The simulations considered use present concentrations of greenhouse gases (Table 1). In HiRes, the same model parameters are used. No specific tuning was needed to equilibrate the surface flux. A larger resolution change would probably implies a specific parameter tuning.

For CTRL, the initial state of the ocean is rest, with temperature and salinity set to the values of the Levitus (1982) atlas at 1 January. Initial state of atmosphere is a 1 January of the ERA15 reanalysis from ECMWF (http://www.ecmwf.int/research/era/ERA-15). The soil model starts with a water content of 300 mm, and no snow cover.

Table 1 Concentration of greenhouse gases used in all experiments 24

CO_2	348 ppm
CH_4	1,650 ppb
N_2O	306 ppb
CFC11	280 ppt
CFC12	484 ppt

HiRes branches off CTRL at year 213, using the ocean and sea ice states of CTRL. Atmosphere, soil and snow over land and land ice restart from the same initial states as the one used for CTRL. Both simulations end at year 500. The mean state and the mean seasonal cycle of years 401–500 are used for all diagnoses.

3.2 Model adjustment

CTRL exhibits three main phases of adjustment (Fig. 2). First, fluxes at top of atmosphere (TOA) and at surface
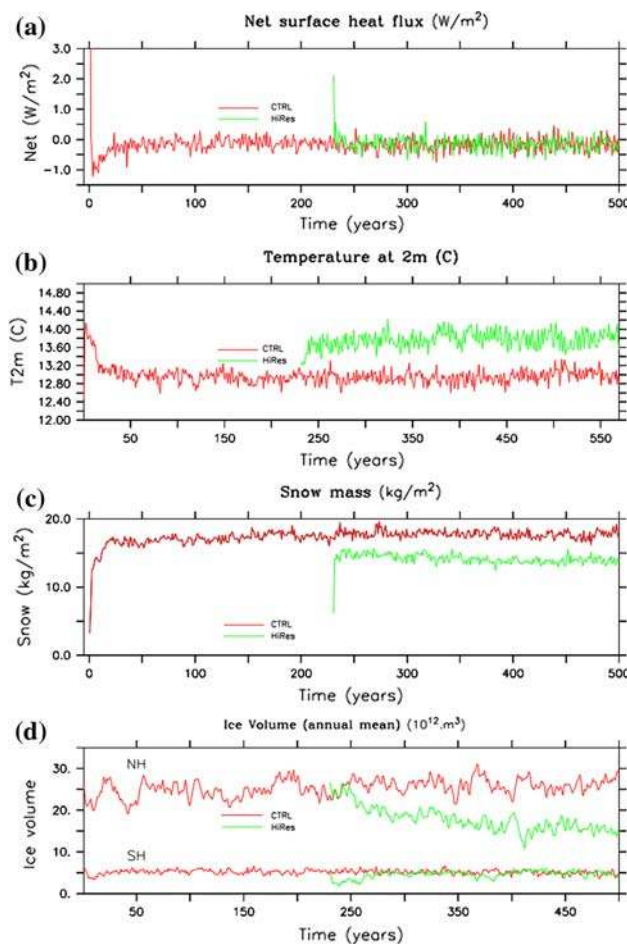
Fig. 2 Evolution of global and annual averages of **a** net surface heat flux (W m^{-2}), **b** temperature at 2 m (C), **c** snow mass (kg m^{-2}). **d** ice volume (10^{12} m^3) for Southern hemisphere (SH) and Northern hemisphere. *Red* for CTRL and *green* for HiRes

adjust rapidly, in about 2 years, and so does surface temperature. During this period, about half of the final snow cover is built. During the next 20 years, the snow cover and the sea ice continue to accumulate to reach almost their final state. Ocean topmost layers (the top 100 m) stabilize within the same time frame. The final stabilization period lasts about 150 years, corresponding to a slow decrease of the ocean transport in the Atlantic, and to an increase of the snow cover in the Northern Hemisphere. Sea–ice increases (not shown), with a strong inter-annual variability. The upper 600 m of the ocean stabilizes during this period. After this adjustment, the model drift becomes negligible, with a global heat budget of -0.15 W m^{-2} at the surface. The global ocean temperature drift is 0.5°C/millennium.

HiRes branches from CTRL with a spun-up ocean and sea ice, but with no snow cover. The stabilization of HiRes also shows three phases, with similar time scales as for CTRL. The snow cover builds up rapidly, but with a reduced extend compared to CTRL (Fig. 2). Surface variables (temperature, albedos, etc.) stabilize within a few years from 90°S to 30°N, which explains why the surface budget adjusts very rapidly (Fig. 2). From 30°N to 90°N,

the adjustment of temperature, snow cover and sea–ice is slower, and takes about 100 years in the Arctic. HiRes stabilizes with a warmer globally averaged temperature (by 0.87°C) than CTRL (Table 2). The drift of temperature and salinity in the deep ocean (below 1,000 m) are detailed in Table 3. They are lower than 0.6°C/millenium and 0.1 PSU/millenium for both experiments in all basins.

The difference in the adjustment of HiRes and CTRL is driven by differences in surface albedo induced by reduced snow and sea–ice cover in HiRes over most of the continental regions in the northern Hemisphere and in the high latitudes (Fig. 3). These surface changes over the continent are mainly due to differences in the large-scale atmospheric circulation. Along 40°S the differences seen in Fig. 3 correspond to a southward shift of the major pattern of the circulation and are discussed in Sect. 4.3. The differences in albedo and temperature are consistent with more solar radiation entering the system in HiRes (3.18 W m^{-2}) and more infrared radiation emitted to space (3.24 W m^{-2}). The difference in clear sky solar radiation at the surface between the two experiments (2.61 W m^{-2}) is similar to the clear sky change in short wave (SW) at the top of the

Table 2 Global averages of heat fluxes and albedos

| Variable	CTRL	HiRes	HiRes–CTRL
Air temperature at 2 m (°C)	12.89	13.85	0.87
Net heat budget at TOA (W m^{-2})	-0.068	-0.125	-0.06
Net short wave at TOA (W m^{-2})	236.5	239.7	3.18
Net long wave at TOA (W m^{-2})	236.6	239.8	3.24
Net heat budget at surface (W m^{-2})	-0.17	-0.15	0.015
Net short wave at surface (W m^{-2})	168.8	171.9	3.17
Net long wave at surface (W m^{-2})	-67.4	-67.8	-0.40
Sensible heat flux (W m^{-2})	-26.1	-25.9	0.25
Latent heat flux (W m^{-2})	-75.6	-78.7	-3.02
Planetary albedo	0.34	0.33	-0.01
Surface albedo	0.16	0.15	-0.01
Precipitable water (g kg^{-1})	22.74	23.87	1.13
Atmospheric greenhouse effect (W m^{-2})	124	125	1.82
LW cloud radiative forcing surface (W m^{-2})	31.67	31.1	-0.54
SW clear sky surface (W m^{-2})	223.5	226.1	2.61
SW clear sky top (W m^{-2})	54.0	51.2	2.8
LW cloud radiative forcing top (W m^{-2})	-50.77	-50.4	0.36

Atmospheric green house effect is computed as $\sigma T_s^4 - LW_{top}$, where σ is Stefan's constant, T_s is the surface temperature and LW_{top} the net long wave flux at top of atmosphere

Table 3 Drift of temperature and salinity in the deep ocean, averaged between 1,000 m and bottom, for global ocean and Atlantic, Pacific and Indian basins

	Temperature (C/millennium)				Salinity (PSU/millennium)			
	Global	Atlantic	Pacific	Indian	Global	Atlantic	Pacific	Indian
CTRL	0.6	0.7	0.5	0.6	0.05	0.05	0.04	0.09
HiRes	0.07	0.2	0.2	0.1	0.07	0.1	0.05	0.07

The drift is computed from basin averages from year 401–500, the period being used for all analyses

Fig. 3 Difference between HiRes and CTRL in latitudinal distribution (annual mean) of **a** heat flux at TOA (*red* short wave, *green* long wave, *black* net), **b** heat flux at the surface (*red* short wave, *green* long wave, *black* sensible, *blue* latent), **c** planetary (*black*) and surface (*red*) albedos, **d** air temperature at 2 m
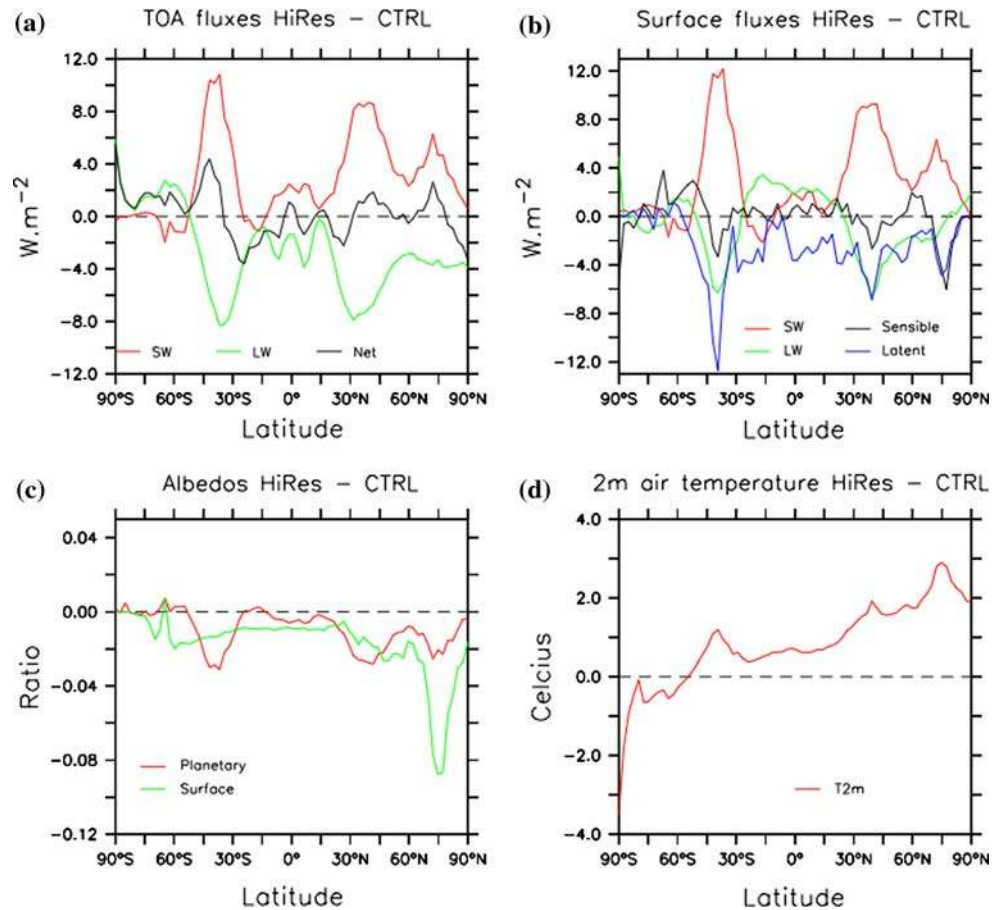
atmosphere (TOA), and represents most of the change in SW radiation. The absorption of the atmospheric column and the cloud radiative forcing have thus only a limited contribution to the SW radiative change, suggesting that the changes in solar radiation are driven by surface conditions, and mostly snow and sea–ice. The excess solar energy in HiRes is balanced at the surface by increased evaporation (3.02 W m^{-2}). The other surface heat fluxes do not change significantly between the two experiments. Changes in the atmospheric temperature profile and the water content both contribute to increase the greenhouse effect of the atmosphere by 1.82 W m^{-2}, which also feedback on the temperature adjustment. Here the green house effect is simply estimated by the difference between the surface emission and the long wave heat flux at TOA. It is not possible from our rough estimates to separate the different effects on the longwave radiation.

The difference in the snow cover and the longwave feedback drives most of the difference in the short term adjustment between HiRes and CTRL (Fig. 2). Then the longer time scale (100 years) needed to reach a surface equilibrium in albedo and temperature corresponds to the time needed in HiRes to reduce the sea–ice cover in high

latitudes. It is associated to an increase of the ocean heat transport in the Atlantic (see below).

3.3 Final state

The differences in surface adjustment between the two simulations also affect part of the atmosphere and ocean column. For the atmospheric part of the system, the major differences between the coupled model and observations follow the patterns seen in atmosphere alone simulations (Hourdin et al. 2006). The zonal mean of temperature exhibits a cold bias of about 8°C at 200 hPa in CTRL (Fig. 4). This pattern was attributed to an overestimation of the moisture content at this level in the LMD model, amplified by the coupling with the ocean (Braconnot et al. 2007a, b). There is a systematic shift of the atmospheric structures (jet stream, temperature) toward the equator already seen in atmosphere only simulations (Hourdin et al. 2006). This yields cold mid-latitudes in the atmosphere and the upper ocean in both experiments. In the southern subtropics and high latitudes, the signal penetrates down in the ocean. At other latitudes, the vertical gradient of oceanic temperatures is not steep enough in the model, with too
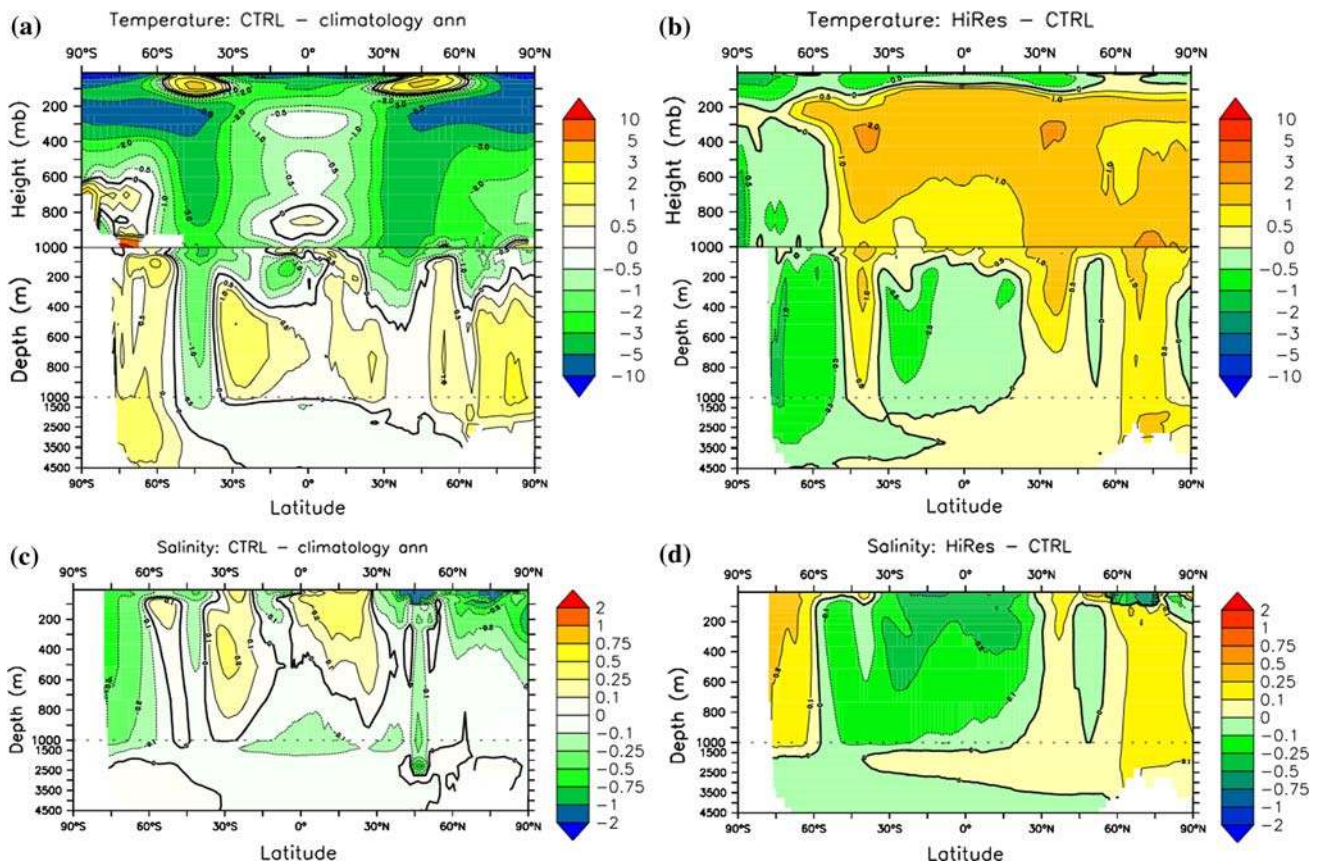
Fig. 4 Zonal and annual means. **a** CTRL minus PHC (Steele et al. 2001) climatology for the ocean temperature, NCEP/NCAR (Kalnay et al. 1996) for the atmosphere temperature. **b** Temperature differences between HiRes and CTRL. **c** CTRL minus PHC climatology (Steele et al. 2001) for the ocean salinity. **d** Salinity differences between HiRes and CTRL. See Table 4 for global averages and Fig. 5 for statistics. PHC climatology merges the 1998 version of the World Ocean Atlas with the regional Arctic Ocean Atlas (Steele et al. 2001)

Table 4 Global averages of key climatic variables, synthesizing the information provided in the figure listed in the rightmost column

Variable	CTRL	HiRes	Data	Data source	See
Air temperature (°C)	−21.47	−20.46	−19.41	NCEP/NCAR (Kalnay et al. 1996)	Fig. 4
Ocean temperature (°C)	3.90	3.87	3.86	PHC (Steele et al. 2001)	Fig. 4
Ocean salinity (PSU)	34.69	34.65	34.72	PHC (Steele et al. 2001)	Fig. 4
SST (°C)	17.35	17.98	18.29	Reynolds (1988)	Fig. 8
Sea surface salinity	34.50	34.35	34.64	PHC (Steele et al. 2001)	Fig. 8
Precipitation, January (mm day^{-1})	2.56	2.69	2.54	CMAP (Xie and Arkin 1997)	Fig. 9
Precipitation, July (mm day^{-1})	2.64	2.74	2.71	CMAP (Xie and Arkin 1997)	Fig. 9
500 hPa height, filtered standard deviation (hPa)	24.6	26.7	26.4	NCEP/NCAR (Kalnay et al. 1996)	Fig. 10
Sea ice, NH, March (10^6 km^2)	13.9	12.3	12.9	Gloersen and Campbell (1991)	Fig. 14
Sea ice, NH, September (10^6 km^2)	5.8	4.2	6.2	Gloersen and Campbell (1991)	Fig. 14
Sea ice, NH, March (10^6 km^2)	6.0	7.0	13.1	Gloersen and Campbell (1991)	Fig. 14
Sea ice, NH, September (10^6 km^2)	15.4	15.1	20.1	Gloersen and Campbell (1991)	Fig. 14
SST, 2°S–2°N (°C)	27.7	28.3	26.8	HadISST1 (1948–1999, Rayner et al. 2003)	Fig. 17
Zonal wind stress, 2°S–2°N (Pa)	−0.016	−0.017	−0.019	ERA40 (1948–2004, Uppala et al. 2005)	Fig. 17

cold surface temperature (except near the equator), and an ocean too warm in the upper 1,000 m. However, the differences do not exceed 1°C in most places. The salinity is too low north of 30°N in CTRL by about 1.5 PSU at the surface. This surface bias extends to about 500, with gradual decrease. This bias has been attributed to the

southward shift of the major pattern of the large-scale ocean circulation and to a too large fresh water input in the north Atlantic (Swingedouw et al. 2006). At 45°N, the fresh water bias at depth corresponds to the Mediterranean outflow, which induces too low salinity at 1,500 m. On the contrary, salinity is too high in the latitudes bands of 0°N–30°N and 15°S–30°S, extending to about 1,000 m.

In HiRes, the moisture content (not shown) is lower than in CTRL below 200 hPa and higher above. The temperature follows this pattern, being colder than CTRL above 200 hPa, and warmer below (Fig. 4), with an exception at high southern latitudes, where temperature remains cooler at all altitudes. The equatorward shift of the atmospheric jet is present but reduced when the atmospheric resolution increases, and so is the temperature bias. Figure 5 synthetizes on a Taylor (2001) diagram the global correlation and the root mean square difference between model and data, and shows that this shift in wind structure slightly improves globally the ocean surface temperature and

salinity. In high northern latitudes, salinities are even smaller than in CTRL near the surface, but larger at depth, with a stronger stratification.

The different equilibria between the two simulations are associated with slight differences in the ocean and atmospheric heat transports (Fig. 6). In CTRL, the global ocean heat transport is correct in the low latitudes, but is too weak north of 20°N and south of 20°S. The value of 1.27×10^{15} W at 24°N is lower than observation-based estimates of $1.8 \pm 0.3 \times 10^{15}$ W (Ganachaud and Wunsch 2003). This weakness appears to be related to the Atlantic heat transport (Fig. 6e). It reaches 0.68×10^{15} W at 24°N in CTRL. Several estimates have been made at this latitude, the lower range being provided by MacDonald (1998) with a $1.07 \pm 0.26 \times 10^{15}$ W estimate. The role of the ocean and of the atmosphere in redistributing heat between the equator and the poles changes between the two experiments, with a more active ocean in HiRes (Fig. 6d). This is attributed to a larger overturning transport in the
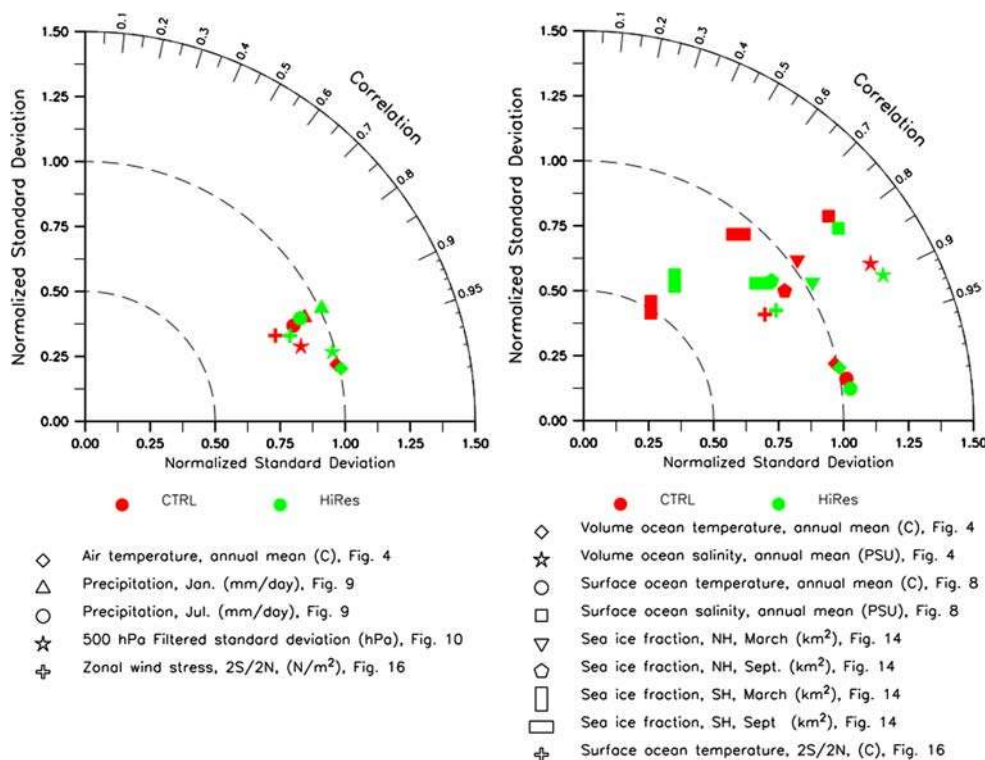
Fig. 5 These Taylor diagrams (Taylor 2001) summarize the standard deviation and the correlation coefficient between model and data. The correlation R is computed between model and data. It is given on the plot by the azimuthal position [i.e. then angle between the abscissa and the line that joints origin to data point is $\cos^{-1}(R)$]. The standard deviation between model and data E' is normalized by the standard deviation of data and the result is plotted as the radial distance to the graphic origin. A high value of the correlation (resp. a low value of the angle) means that the model pattern is close to the data pattern. A normalized standard deviation close to 1 means that the amplitude of the pattern are close in model and data. The centred RMS between

model and data is the linear distance between the observations (always on the abscissa, at radius 1) and the model points. It is a measure of the 'distance' between model and data. CTRL is in *red*, HiRes in *green*. Fields are listed in the figure, with the indication of the *symbol* used, the units of the standard deviation, and the figure to which it refers. *Left panel* is for atmospheric variables and *right* for ocean and sea ice. The data used are detailed in each corresponding figures captions, and in Table 4. For sea ice, the correlation is computed only where sea ice is present either in observation, in CTRL or in HiRes
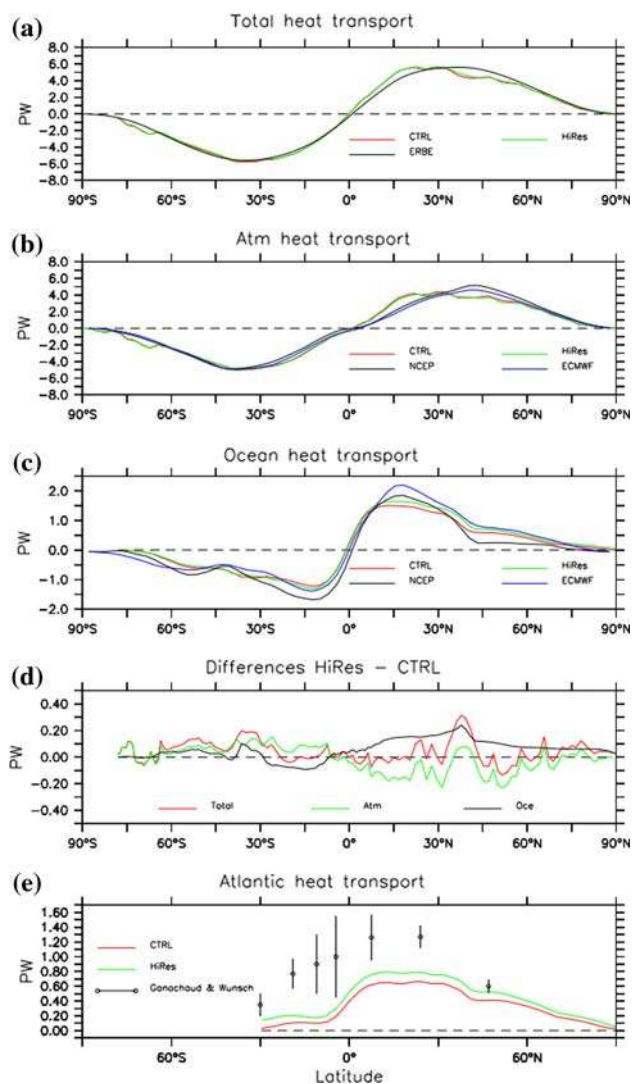
Fig. 6 Annual mean heat transports, for CTRL (*red*) and HiRes (*green*). **a** Total transport (ocean plus atmosphere). The *black line* is the transport implied by the net radiative flux at top of atmosphere (TOA) from ERBE data (Barkstrom 1984). To obtain the transport, the TOA net flux is integrated from the South Pole, and arbitrarily set to zero at the equator. Wunsch (2005) estimated the error to $\pm 1.1 \times 10^{15}$ W at the latitudes of the extrema. **b** Atmospheric heat transport. Estimates from NCEP/NCAR (Kalnay et al. 1996, *black line*) and ERA40 reanalysis (Uppala et al. 2005) have been added. **c** Ocean heat transport. Estimates from Trenberth and Caron (2001) has been added (*black line*). **d** Differences between model and observations. **e** Atlantic heat transport. *Estimates* and *error bars* from Ganachaud and Wunsch (2000) has been added

Atlantic (see below). In HiRes, the ocean heat transport north of 10°N reaches a maximum of 1.49×10^{15} W, and an Atlantic maximum of 0.82×10^{15} W.

The stream functions of the zonally integrated ocean flow of the present day equilibrium simulations (Fig. 7) reflect the underestimation of the ocean heat transport (Fig. 6). Even though it is in good qualitative agreement with observations in CTRL (e.g. Ganachaud and Wunsch

2003; Talley et al. 2003), the maximum value of about 11 Sv (1 Sv $\equiv 10^6$ m^3 s^{-1}) is too small. The maximum strength of the AMOC increases in HiRes and reaches 15 Sv. This is still not sufficient to ensure a realistic northward heat transport but it is not inconsistent with the observational estimates cited above. Apart from this intensification, the NADW cells are similar in the two simulations. In particular, the cell reaches the same depth, approximately 3,000 m. At depth, the AABW is hardly affected by the change in atmospheric resolution. It is weak in both cases.

Following Bryden and Imawaki (2001), we separate the oceanic heat transport between its barotropic part (gyre heat transport) and its baroclinic part (overturning heat transport). The gyre heat transport is very similar in the two simulations, with values of 0.19×10^{15} W and 0.17×10^{15} W for CTRL and HiRes, respectively, while the overturning heat transport significantly increases from 0.49×10^{15} W in CTRL to 0.66×10^{15} W in HiRes. The increase in the Atlantic heat transport with increasing atmospheric resolution is therefore mostly due to the improvement of the AMOC intensity (see section 0 for the explanations concerning this improvement). Note that, according to Boning et al. (1995), every increase of 2 Sv in AMOC is associate to an increase of 0.1×10^{15} W in heat transport at 25°N. An AMOC intensity of 18 Sv at 25°N will be necessary to obtain a 1.1×10^{15} W ocean heat transport. This value is in agreement with Talley et al. (2003) estimates. It shows that in our simulations the bias in AMOC intensity (8.3 Sv and 4.5 Sv at 25°N in CTRL and HiRes, respectively) is consistent with the bias in ocean heat transport.

3.4 Surface characteristics

Figure 8a shows the difference between the simulated annual mean sea surface temperature (SST) and the Reynolds (1988) climatology. Both simulations capture successfully the large-scale patterns. The main shortcoming of CTRL is a cold bias at middle latitudes both in the Atlantic and the Pacific oceans. The bias reaches 6°C in the North Atlantic, resulting from a combination of a southward shift of the north Atlantic drift and the advection of cold water from the north. At higher resolution (HiRes), the bias is strongly reduced in both oceans and both hemispheres.

In the tropics, temperature and salinity biases are found in the eastern part of the basins in the Atlantic and the Pacific, and along the continental boundaries in the Indian Ocean. This is a typical bias in coupled ocean–atmosphere models (IPCC 2007, Fig. S8.1). It is associated with insufficient resolution, which leads to a poor representation of the local wind stress and the oceanic upwelling (Braconnot et al. 2007a, b).

Fig. 7 Stream function of the Atlantic meridional overturning. *Left* CTRL, *right* HiRes. Isoline every 2 Sv, and every 10 Sv above 20 Sv
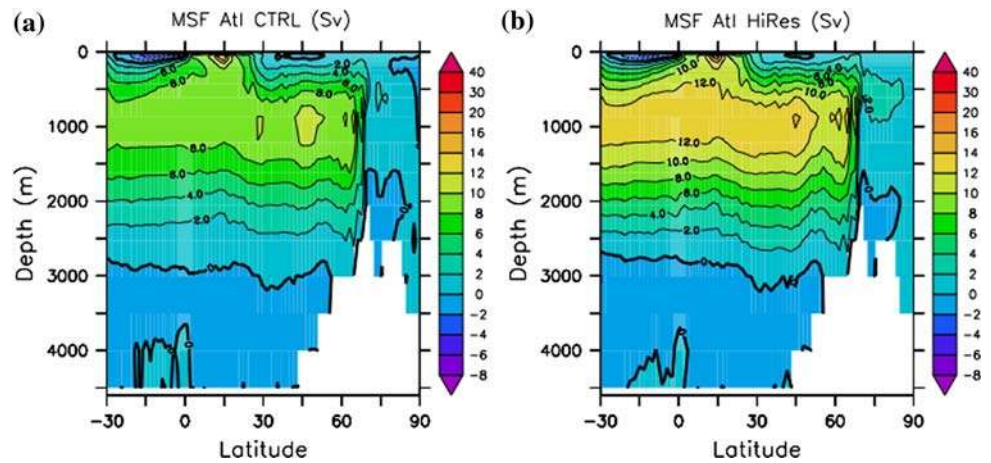
Fig. 8 a Difference between CTRL simulated sea surface temperature (annual mean) and the climatology of Reynolds (1988). Isolines are plotted every 1°C. **b** Difference between HiRes and CTRL SST. Isolines are plotted every 0.5°C. **c** Difference between CTRL simulated sea surface salinity (annual mean) and the PHC (Steele et al. 2001) climatology. Isolines are plotted every 0.5 PSU. **d** Salinity differences between HiRes and CTRL. Isolines are plotted every 0.25 PSU. See Table 4 for global averages and Fig. 5 for statistics
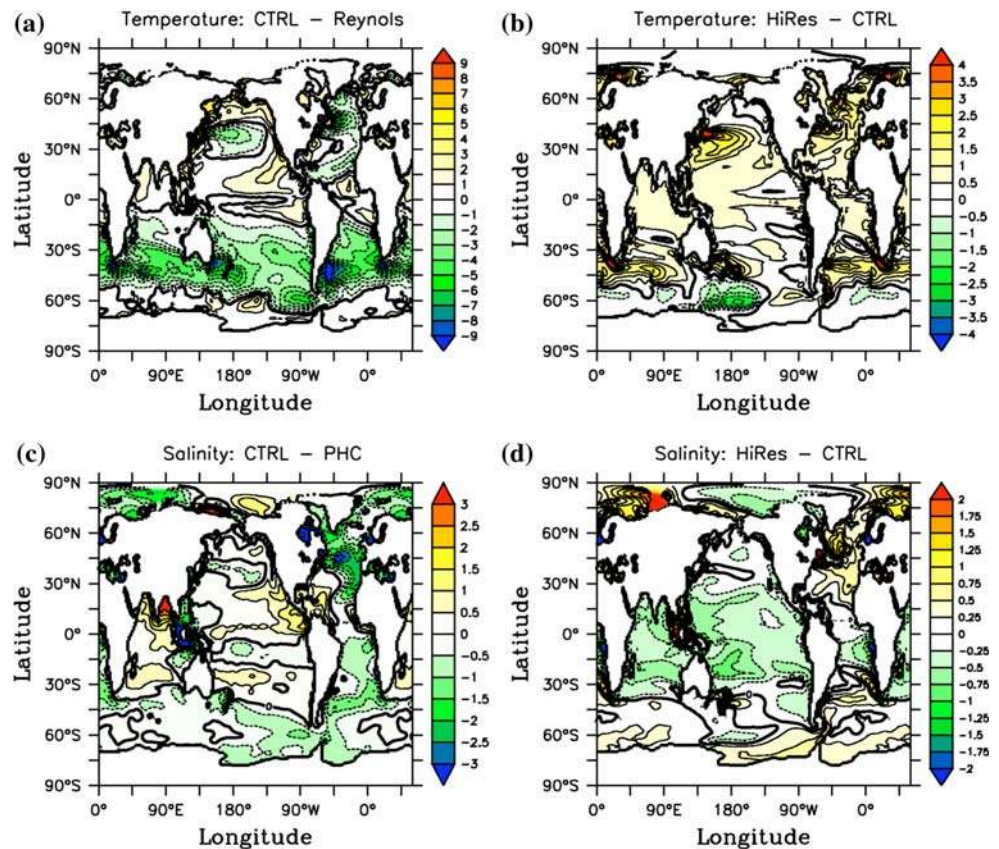
The combination of the cold bias at middle latitudes and the warm bias in the tropics is associated to a stronger than observed equator-to-poles SST gradient. The gradient is improved with enhanced atmospheric resolution, suggesting that increasing the resolution has corrected some circulation errors. This differs from Hack et al. (2006a, b) who find similar SST error patterns and magnitudes in versions of the CCSM3 with atmospheric configurations T42 and T85, respectively.

The large-scale characerics of precipitation (Fig. 9) in CTRL are detailed by Braconnot et al. (2007a, b). They

are consistent with the temperature field. In January, precipitation north of the equator in the eastern Pacific is too sluggish, with even less precipitation in HiRes. The double ITCZ (intertropical convergence zone) at 4°S is present in both simulations, and is stronger in HiRes. The structure of the South Pacific Convergence Zone is too zonal in both simulations, penetrating too far toward the east Pacific. In the Atlantic, ITCZ precipitations are too weak in January, particularly over the Amazon. In July, the ITCZ of CTRL is shifted southward compared to observations. Its position is better represented in HiRes,

Fig. 9 January (*left*) and July
(*right*) precipitation (in
mm day^{-1}) for CMAP (Xie and
Arkin 1997) data (*top*), CTRL
(*middle*) and HiRes (*bottom*).
See Table 4 for global averages
and Fig. 5 for statistics
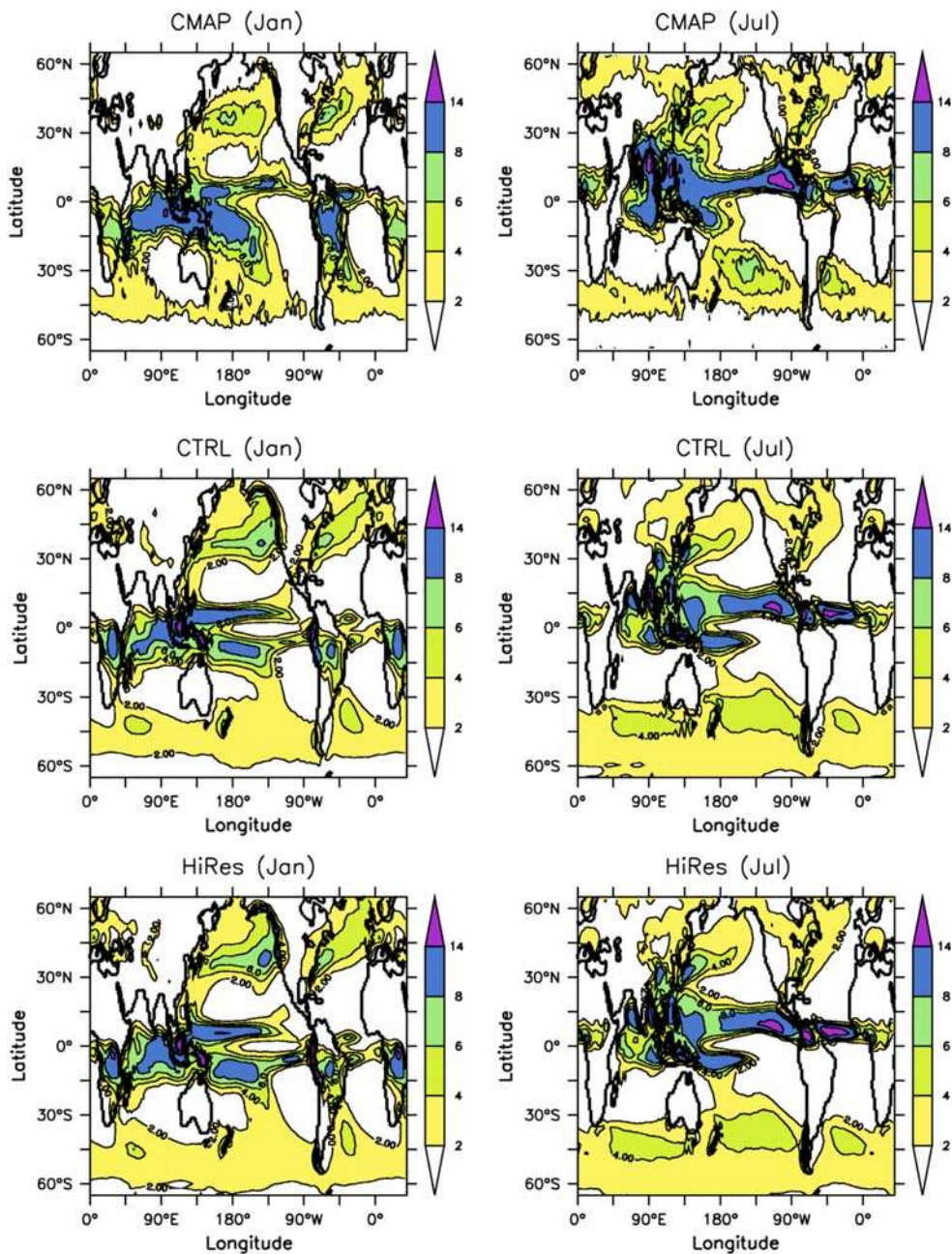
with stronger rainfall along the Africa coast. However, HiRes does not improve the monsoon rainfall over Africa.

The large-scale characteristics of the two simulations are summarized in Table 5 and Fig. 5. The larger improvement between CTRL and HiRes is obtained for sea ice in the southern hemisphere. Other fields also benefits from measurable improvement. It concerns mainly the dynamics of the atmosphere with the zonal wind stress and the 500 hPa filtered standard deviation. Over the ocean, temperature benefits from larger improvements than salinity.

Table 5 Comparison of the fresh water budget (in mSv $\equiv 10^3$ m^3 s^{-1}) of different simulations with climatology of continental runoff discharge from UNESCO and evaporation minus evaporation ($E - P$) from ERA40 (Uppala et al. 2005), north of 40°N in the Atlantic and Arctic Ocean

	CTRL	HiREs	ERA40
Runoff (10^3 m^3 s^{-1})	−221.8	−196.8	−200.1
$P-E$ (10^3 m^3 s^{-1})	−232.1	−246.7	−134.0
Sea ice (10^3 m^3 s^{-1})	−6.2	−6.7	not available
Total (10^3 m^3 s^{-1})	−460.1	−450.2	−334.1

4 Regional characteristics and role of processes and feedback related to the atmospheric resolution

This part focuses on the climate of specific regions to address the impact of the atmosphere resolution on regional processes and feedbacks. In the North Atlantic, wind structure and variability have a strong impact over the ocean deep convection and thermohaline circulation. At high southern latitudes, the Antarctic Circumpolar Current responds to the structure and strength of winds. In the tropics, atmosphere resolution changes the seasonal cycle and the ENSO variability.

4.1 North Atlantic atmospheric circulation

Most of the differences in the Atlantic sector between CTRL and HiRes may be attributed to differences in the winds. Mid-latitude climates are characterised by their day-to-day variability, especially in winter over the oceans and surrounding regions (Hoskins and Hodges 2002). The phenomena responsible for this variability are the weather systems that develop over the Pacific and Atlantic oceans. They are responsible for a large part of the precipitation and of the equator-to-pole heat transport at these latitudes. Due to their typical size, of the order a thousand km, and to the present resolution of climate models, the representation of the variability associated with these weather systems is expected to be sensitive to resolution. For example, Dong and Valdes (2000) show that increasing the resolution from T21 to T42 leads to major improvements of the storm-track representation, in particular in the amplitude of the storm-track. A further increase to T63 resolution does not yield such a strong effect, showing that T42 is a threshold resolution. The resolutions of our experiments, 96×72 and 144×96 straddle this threshold and we expect significant differences in the storm-track representation in the simulations.

Figure 10 shows the high-pass filtered 500 hPa geopotential height standard deviation computed from the NCEP/NCAR reanalyses and the CTRL and HiRes simulations. The filter is Hoskins and Hodges (2002) 'poor-man filter' retaining variability for periods smaller than 10 days. The figure shows that even at a medium resolution (CTRL) both storm-tracks are quite well represented. However, the Pacific storm-track is not strong enough and does not present a secondary maximum near the American coast. In CTRL, the Atlantic storm-track has, as in the NCEP/NCAR reanalyses, a stronger maximum than the Pacific storm-track, but this maximum is smaller than in the reanalyses and the region of high variability does not extend as much to the Northeast, over the Norwegian Sea, as in the reanalyses. Both the amplitude and the longitudinal extent of the storm-tracks are better represented in HiRes. The

Pacific storm-track is even a little too strong. The Atlantic storm-track's amplitude, on the other hand, is satisfactory but its eastern end tilts too much to the south compared to the reanalyses. The two simulations also differ over Siberia, with a larger variability, closer to the reanalyses, in the high resolution case.

The increased resolution therefore results in a better representation of the winter mid-latitude storm-tracks, which can relate to a slightly improved representation of the equator-to-pole transport shown on Fig. 6. Storm-tracks are related to equator-to-pole temperature gradients through baroclinic instability theory. In Sect. 3.4, we have shown that this gradient is too strong in the low resolution run, while it decreases and is more similar to the observed one in the high resolution run. So, the increase in storm-track variability in the high resolution run is not related to an increased equator-to-pole thermal gradient, but rather, probably, to the resolution itself. The improvement of the representation of the precipitation over the East Atlantic could also be related to these improvements in the storm-tracks.

Another approach to diagnose the effect of the resolution on atmospheric circulation is to assess the North Atlantic oscillation (NAO) variability in the two experiments. A large number of spatial patterns and indices have emerged in studies of the northern hemisphere wintertime low-frequency variability. Recently, Quadrelli and Wallace (2004) have shown that they can all be almost fully retrieved by a linear combination of only two basis patterns: the leading two empirical orthogonal functions (EOF) of the monthly sea level pressure (SLP) field. The first two EOFs computed by a principal component analysis of the NCEP/NCAR reanalysis SLP for the 1958–2007 period are shown on the left panels of Fig. 11. EOF1 is a quasi-zonally symmetric dipole between the polar and mid-latitude also called the Northern Annular Mode or Arctic Oscillation. EOF2 on the other hand is a wavy pattern with a large centre of action over the Pacific and a weaker secondary wave train over Europe. The two EOFs are orthogonal by construction.

The first EOF of SLP for the CTRL and HiRes simulation is similar to the observed one (Fig. 11). Over the Atlantic sector, they all resemble the NAO pattern, although the structure is shifted slightly northward and stronger over Siberia in the simulations. The main difference is over the Pacific Ocean: in CTRL the EOF1 variance is concentrated in the Atlantic, whereas in HiRes and the reanalysis there is a secondary centre of action in the Pacific of comparable amplitude. The second simulated EOF exhibit the dominant Pacific centre, shifted to the east in both cases. The wave train over the Atlantic is however better captured by HiRes, where it is in phase with the observed one, instead of phase quadrature for CTRL. These

Fig. 10 High-pass filtered standard deviation of the 500 hPa geopotential height for DJF (units: hPa). *Top* NCEP/NCAR Reanalyses (1980–1999, Kalnay et al. 1996), *middle* CTRL, *bottom* HiRes. See Table 4 for global averages and Fig. 5 for statistics
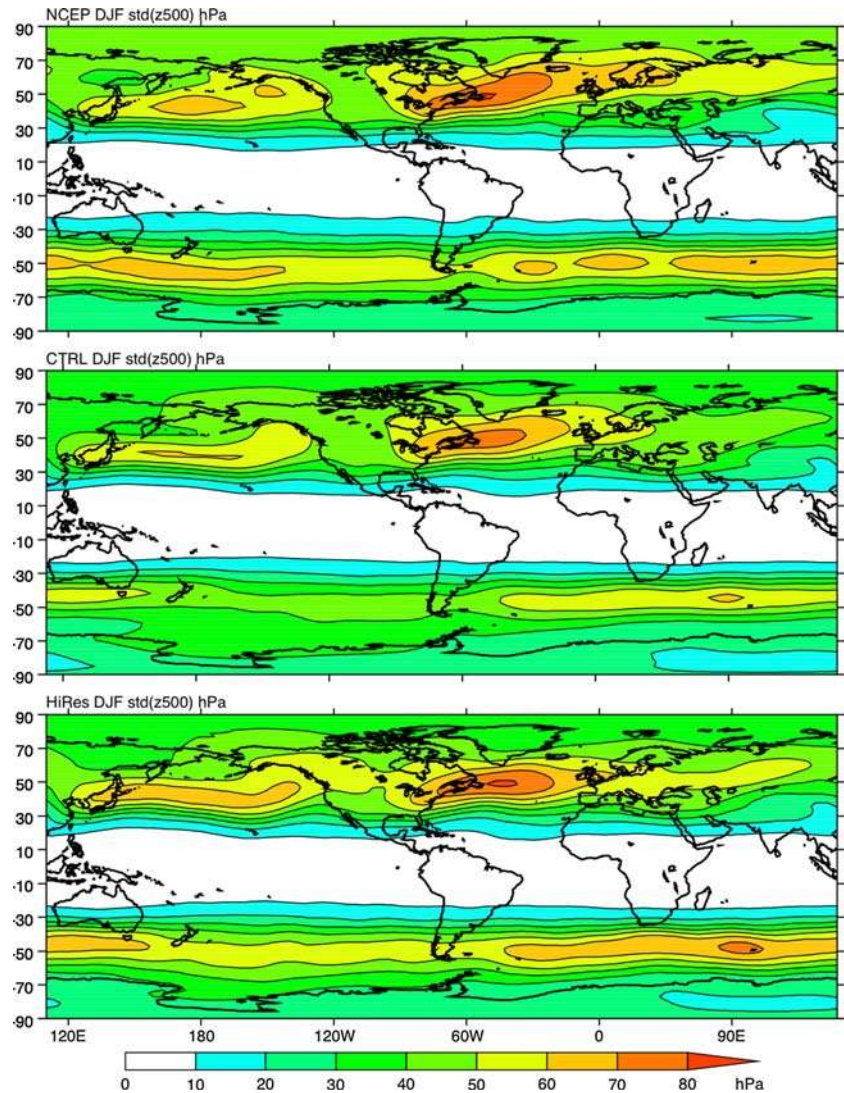
results can be summarized by Fig. 12, following Quadrelli and Wallace (2004): each simulated EOF is represented by a line whose projections on the horizontal and vertical axes give the spatial correlation with the observed EOF 1 and 2, respectively. The HiRes EOFs reproduce almost perfectly the observed ones (the correlation of EOF 2 with NCEP/NCAR EOF2 is not perfect, because of the small shift of the Pacific centre, but the orthogonality with the EOF1 is conserved). For CTRL, EOF1 and 2 are rotated with respect to the NCEP ones: this reflects the poorer representation of the Pacific/Atlantic connections in this simulation.

There is therefore a strong improvement with resolution of the simulated variance in the Pacific, and its connection with the Atlantic sector. A possible reason is that the Pacific jet is stronger than the Atlantic one, and driven to a large extent by tropical heating. An even stronger jet, as found in lower resolution simulations (not shown) will tend to trap eddies and destroy the positive feedback between

eddies and jet fluctuations at the origin of the observed low-frequency variability (Eichelberger and Hartmann 2007). This mechanism is consistent with a continuous decrease of the Pacific jet speed from CTRL to HiRes, and a corresponding increase in storm-tracks amplitude and month-to-month sea level pressure variance. This is consistent with an improvement of the wind structure, and its effects on the gyre circulation (see below).

4.2 Oceanic circulation in the North Atlantic

The improvement of the atmospheric circulation in HiRes has a strong impact on the characteristics of the Atlantic Ocean, including the representation of sea ice cover, deep-water formation and thermohaline circulation. In the Northern Hemisphere, the sea ice concentration is overestimated in CTRL during wintertime in the Atlantic sector, with sea ice covering the Labrador and Barents Seas (Fig. 14a). The maxima in ice thickness are situated north

Fig. 11 First (*top*) and second (*bottom*) empirical orthogonal functions (EOF) computed by a principal component analysis of the sea level pressure. *Left* NCEP/NCAR (Kalnay et al. 1996) reanalyses, *middle* CTRL, *right* HiRes
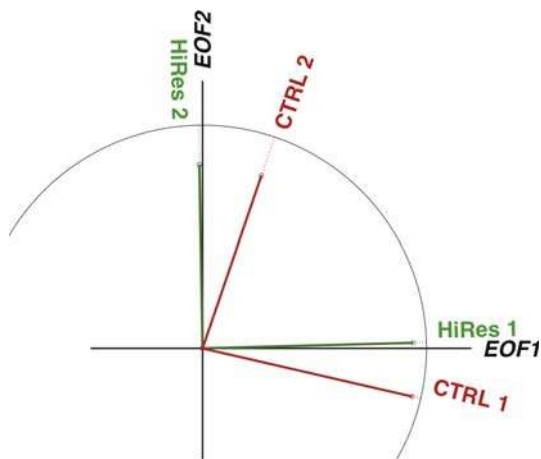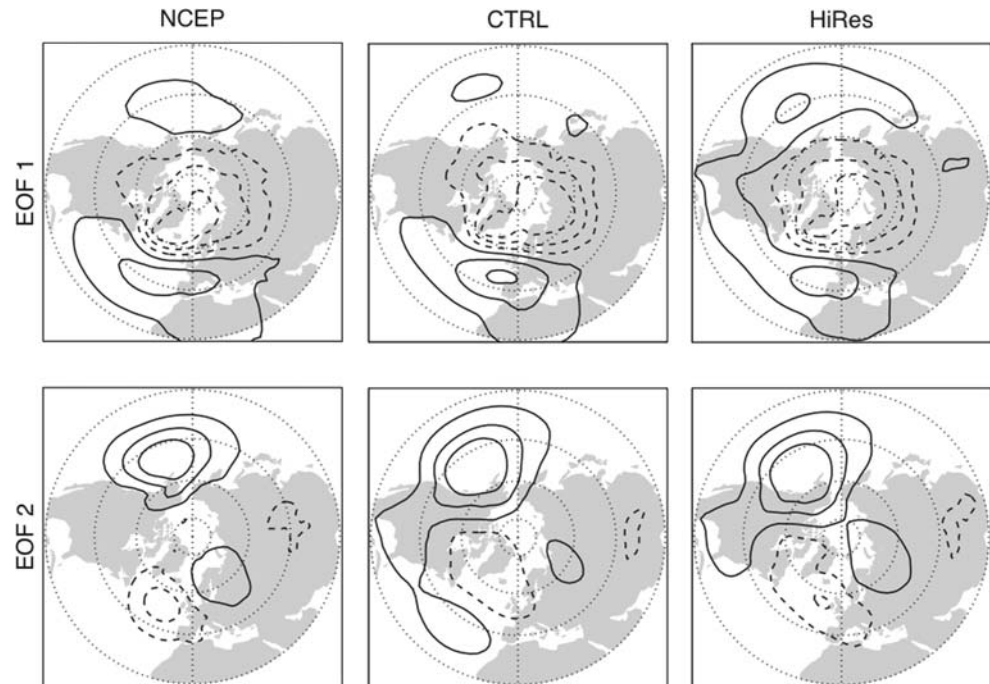
Fig. 12 Correlations between observed and simulated EOF of SLP. See *text* for details

of the Canadian Archipelago and north of Greenland (Fig. 14a), in good agreement with observations (Bourke and McLaren 1992). A less realistic secondary maximum is present in the eastern Siberian Sea. On the other hand, a slight underestimation of the winter sea ice extent in the Okhotsk and Bering Seas is present (Fig. 14c). The underestimation of the ice extent is still present in summer in HiRes in the North Atlantic, the GIN seas (Greenland–Icelandic–Nordic seas), and the Barents Sea (Fig. 14d). There is almost no difference with respect to CTRL in the Bering and Okhotsk Seas. HiRes has a more realistic ice thickness distribution in the Arctic, in particular in the eastern Siberian Sea where CTRL simulates an ice

thickness higher than 6 m. The reduction of the bias there in HiRes is due to a better location of the Beaufort high in this model version. Indeed, in CTRL, the high pressure system in the Canadian Basin extends towards the North Siberia (not shown), resulting in onshore winds that transport sea ice towards the eastern Siberian Sea and induce a high sea ice accumulation there. DeWeaver and Bitz (2006) found the same type of reduction of model biases when comparing CCSM3 simulations at high and medium resolutions. They attribute this improvement to a better representation of the fall and winter Arctic surface winds in the high resolution version of the model.

The sea ice off the Labrador Sea is reduced in HiRes, but still extends too far east. Because of a stronger northward oceanic heat transport in the northern North Atlantic (Fig. 6e), the overestimation in sea ice extent in the North Atlantic sector seen in CTRL is strongly attenuated in HiRes, leading to a reasonable sea ice edge position in winter characterized by only small errors in the central Labrabor Sea and north of Iceland. The improved ocean heat transport in HiRes is associated with differences in the location and intensity of deep-water formation. The model deep-water formation is characterised by two sites of deep convection in the North Atlantic (Fig. 13). One site is located in the Nordic Seas, as in the observations, although the site is shifted to the south-east in the model as compared to observations and the maximum of the mixed layer depth is not deep enough (Swingedouw et al. 2006; Swingedouw et al. 2007). Both discrepancies are reduced in HiRes. The location of deep convection south of Iceland in both simulations is unrealistic, while there is no deep

Fig. 13 Maximum depth of the mixed layer in meter. Isolines every 250 m. The *thick red lines* show the winter and summer position of the sea ice edge (limit of 15% of sea ice concentration). **a** Data from de Boyer Montégut et al. (2004) for the mixed layer and Gloersen and Campbell (1991) for the ice edge. **b** Difference between HiRes and CTRL. *Full colors* correspond to the 99% Student test significant differences. **c** CTRL. **d** HiRes
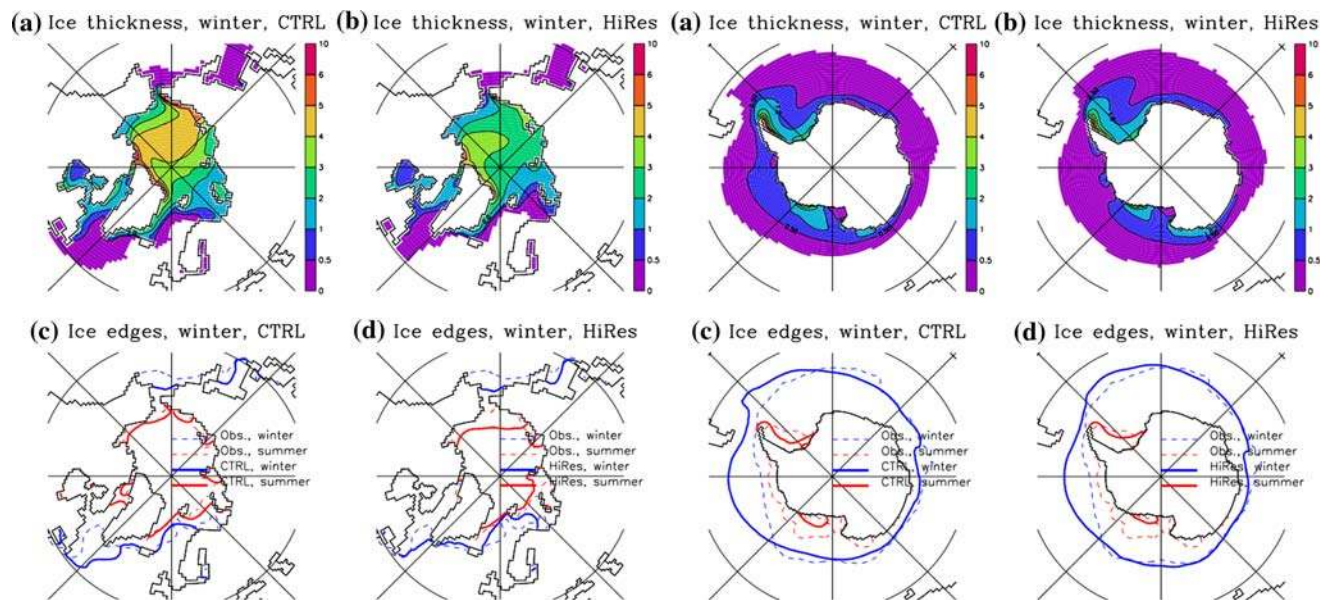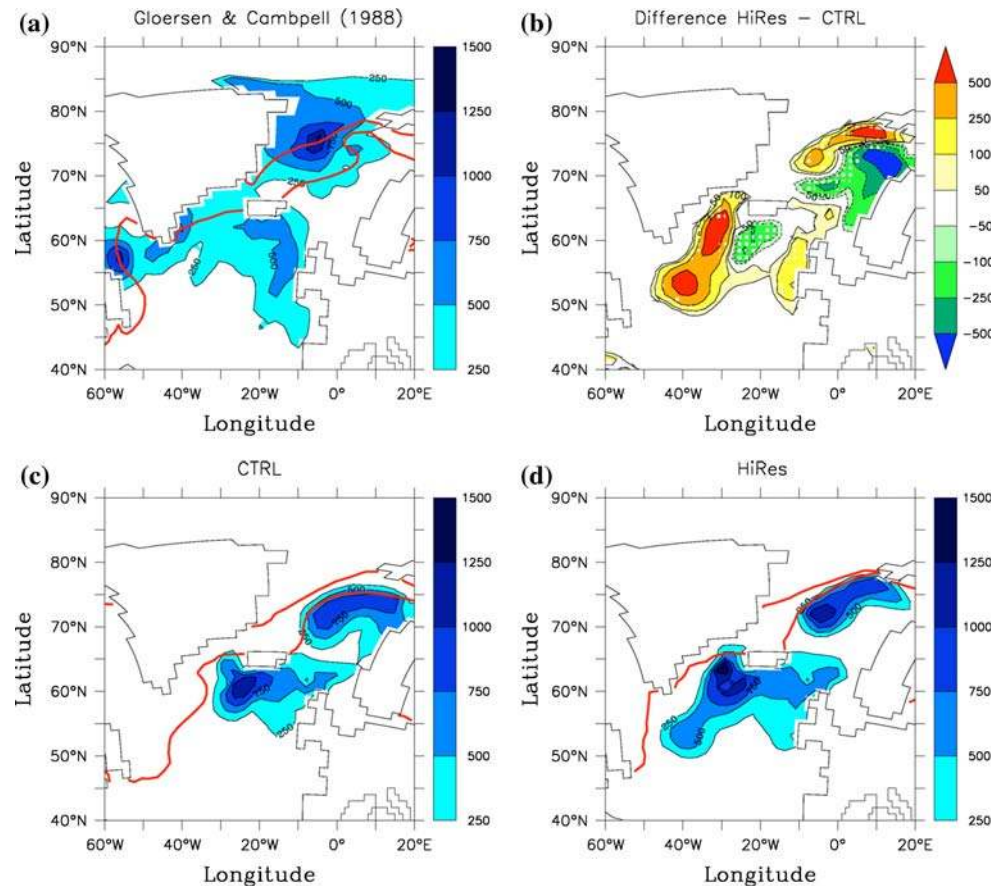
Fig. 14 Winter sea ice thickness for the model (*top*), and winter and summer ice edges (*bottom*) for model and data (Gloersen and Campbell 1991). See Table 4 for global averages and Fig. 5 for statistics

convection in the Labrador Sea in the model. As discussed in Swingedouw et al. (2007), this is presumably due to an excess of fresh water input in the northern North Atlantic.

As a result of this lack of convection in the Labrador Sea, this basin is fully covered by sea ice in winter, contrary to what is observed. The increase of atmospheric resolution

induces a slight northward shift of the winter sea ice limit in the Labrador Sea, but this is still not sufficient to allow deep convection in the Labrador Sea. In agreement with the deepening of maximum mixed layer depths in the northern North Atlantic, Atlantic MOC is stronger in HiRes and reaches 15 Sv (Fig. 7).

In both simulations and at both convection sites, an increase of sea surface density and mixed layer depth is correlated to increased sea surface salinity. In the model, deep convection is thus primarily driven by haline anomalies. SST is hardly correlated with sea surface density anomalies in these areas (except south of Iceland in CTRL, but with a sign of correlation that would rather prevent deep-water formation).

Changing the resolution can affect the atmospheric dynamics and cloud distribution, which therefore can modify the water budget. Nonetheless, Hack et al. (2006a, b) did not manage to correct the global precipitation bias by increasing horizontal resolution. Here we focus on the atmospheric fresh water forcing of the Atlantic, north of 40°N for the different model resolutions in comparison with the data from ERA40 (Uppala et al. 2005) and UNESCO rivers data (Table). We notice that increasing the resolution does not significantly modify the total surface fresh water budget in the region analysed. A total bias of more than 0.1 Sv in comparison with the observations appears in both atmospheric resolutions. This bias is mostly related to an incorrect budget of precipitation minus evaporation in the northern high latitudes. The difference in terms of salinity in the North Atlantic and AMOC between HiRes and CTRL is therefore not attributable to differences in surface fresh water forcing and is therefore certainly related to salt transport.

Following Wijffels et al. (1992), we separate the salinity transport into a gyre component primarily related to the barotropic part of the transport, and an overturning component related to the baroclinic part. The overturning salt transport depends on the AMOC intensity. It represents a classical positive feedback for the AMOC (Stommel 1961), which cannot be the trigger for an increase in salinity in the convection sites. Gyre salinity transport is related to the barotropic stream function, which strongly intensified when the atmosphere resolution increases (not shown). This salinity transport related to the gyre is represented in Fig. 15 for both resolutions in the Atlantic basin. The gyre salt transport reaches 15.9×10^6 kg s^{-1} at 50°N in HiRes and 9.9×10^6 kg s^{-1} in CTRL. This 50°N latitude is of paramount interest since the convection sites are very close and their salinity may therefore be highly sensitive to this transport. Thus, the 59% enhancement in gyre salt transport certainly explains most of the increase in salinity observed in HiRes compared to CTRL.
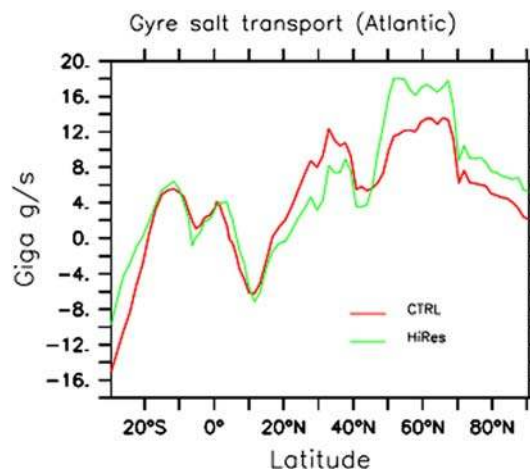
Fig. 15 Salt transport (10^6 kg s^{-1}) by the gyre component for CTRL (*red*) and HiRes (*green*). See Appendix A.2 for the computation of the gyre component

4.3 Southern latitudes

In the southern hemisphere, the latitude of the observed zonal wind stress maximum is close to the latitude of the southern tip of America (~ 55°S, see Fig. 16). In CTRL, the zonal wind stress is weaker than in observation, with a maximum at 43°S, and the location of the zero wind stress curl is shifted northward. The wind stress in the 55°S–65°S latitude band is weak compare to observation. This yields a weak Antarctic Circumpolar Current (ACC, see Fig. 16), with a volume transport at Drake passage of 50 Sv, which is much lower than the observational estimate of 136.7 ± 7.8 Sv (Cunningham et al. 2003). In HiRes, the wind stress maximum is improved, and the latitude of the maximum is shifted southward at about 48°S. The zero of the wind stress curl is also shifted southward (not shown). Following (Russell et al. 2006), this yields a more southward location of the ACC in HiRes. The ACC is strengthened, with transport of 80 Sv through the Drake Passage.

In the Southern Ocean, both model versions tend to overestimate the amplitude of the seasonal cycle of the sea ice extent (Fig. 14), with sea ice almost vanishing in summer. On the other hand, because of a relatively high oceanic heat flux at the ice base, the winter sea ice thickness in the majority of the seasonal ice pack is quite low, with values lower than 50 cm. Higher values, up to 2 m, are simulated in the Weddell Sea, along the Antarctic Peninsula and the Filchner-Ronne ice shelf, as well as in the eastern Ross Sea.

4.4 Seasonal and interannual variability in the tropics

This last part investigates the changes in the tropical regions. Figure 17 shows the annual mean and mean

Fig. 16 *Left panel* barotropic stream function in Sv in the Southern Hemisphere for CTRL (*red*) and HiRes (*green*). *Right panel* zonal average of the zonal wind stress for CTRL (*red*), HiRes (*green*) and ERA 40 (*black*) (Uppala et al. 2005)
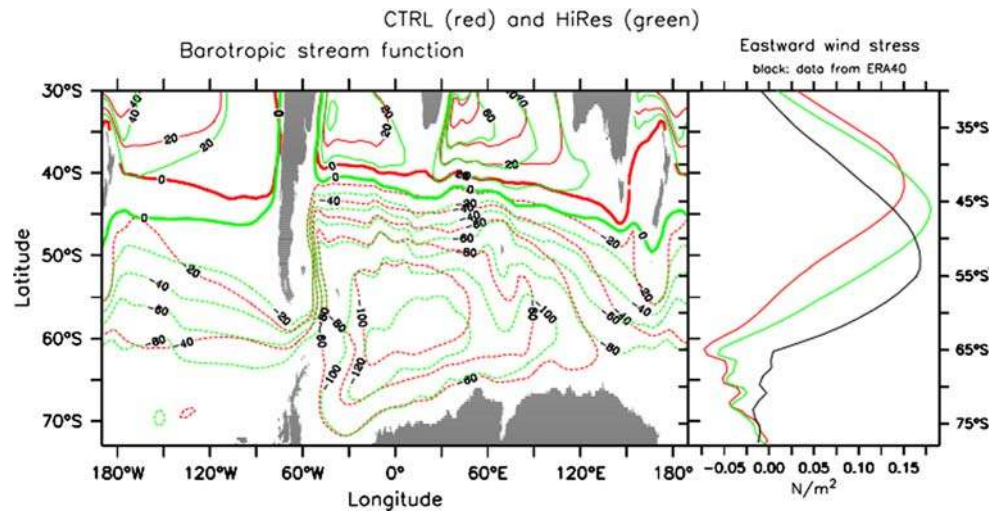
seasonal cycle of SST (annual mean removed) and of the zonal wind stress along the equator, compared to data and reanalyses (references in figure caption). The model is warmer than observed in all basins. In the Pacific and Indian oceans, the east–west SST gradient is correctly represented, with an exception near the Chile coast (Fig. 17, bottom). The Atlantic SST is too warm in the Gulf of Guinea. This is associated with a too flat Atlantic thermocline (Braconnot et al. 2007a, b), too deep in the east, and to a lack of shallow clouds. The HiRes experiment has warmer SST in all basins, with an east–west gradient similar to CTRL. The zonal wind stress is correctly represented in intensity and east–west gradient in the Indian. In the Atlantic, winds are slightly too strong in the middle of the basin. In the Pacific, the east–west gradient is too strong, with a maximum near 160° west not well represented, and too strong eastward winds over the warm pool. The increase in resolution slightly improves the wind structure in the Pacific when compared to ERA40 reanalysis.

In the three basins, the seasonal cycle of SST and wind is correctly phased in both experiments, but the amplitudes are too low (Fig. 17). In the Atlantic, the maximum of SST variability is shifted toward the Brazilian coast. In the Pacific, the SST variability extends correctly from the east, but its westward extension is slightly underestimated. The SST is quite similar to observed ones, except near the Chile coast, where it is too warm. From November to January, southern hemisphere trade winds cross the equator, and a maximum of zonal winds is located around 150°W in ERA40 (Fig. 17b). In the two experiments, this maximum is not present (Fig. 17d, f). The northern hemisphere trade winds penetrate too far south (Braconnot et al. 2007a, b, Fig. 4b), and the southern hemisphere trade winds do not cross the equator. This is consistent with the presence of the double ITCZ structure with a secondary maximum

precipitation around 4°S. These low winds yield a reduction of the equatorial upwelling, and a spurious SST maximum (Fig. 17a, c and e) during this season. SST is well represented in the Indian sector. The resolution does not affect much the phasing and the position of the structures, but slightly improved the amplitude. For instance the temperature maximum in April is improved in all basins. Compared to those of the other CMIP3 models, the seasonal cycle in the east Pacific in IPSL-CM4 is quite well represented, both in phase and amplitude (about 2.7 years vs. 4–5 years in observations, Guilyardi 2006).

The monthly standard deviation of SST (Fig. 18a–c) shows that the ENSO amplitude in CTRL is about right (1.0°C in Niño3[1] vs. 0.85°C for observations). Its structure extends too far to the west and is too confined around the equator (see the 0.40°C contour). This is classical bias of coupled GCMs which tend to have too strong mean zonal wind stress τ_x (Figs. 18g, 2 of Guilyardi 2006). The zonal wind stress variability is too weak in the equatorial band between 10°S and 10°N (about half of the value of the ERA40 reanalysis, see Fig. 18g). The coupling strength, which measures the intensity of the atmosphere dynamical response to a SST anomaly (mostly via the Bjerknes feedback) is key to El Niño development and amplification. It can be diagnosed in coupled GCMs as the slope of the Anomaly of $\tau_{x\ \text{Niño4}} = f(\text{anomaly of SST}_{\text{Niño3}})$ relationship. Here, the weak wind stress variability in CTRL results in a weak interannual coupling strength of 4.3×10^{-3} N m^{-2} K^{-1} instead of 9.5×10^{-3} N m^{-2} K^{-1} in the ERA40 reanalysis (Fig. 18h, see also Guilyardi (Fig. 18h, see also Guilyardi 2006)). This weak coupling strength together with a right amplitude suggests that the processes damping ENSO in the model are underestimated.

---

[1] Niño 3 is the 5°S–5°N/120°W–170°W region. Niño4 is the 5°S–5°N/160°E–150°W region.

Fig. 17 Mean seasonal cycle of the SST (*left panel*) and zonal wind stress (*right panel*), with annual mean removed and averaged between 2°S and 2°N. Isoline every 0.5°C and 0.01 Pa. *Bottom plots* display the annual average of models and data averaged between 2°S and 2°N. Data are from HadISST1 (1948–1999, Rayner et al. 2003) for SST and from ERA40 (1948–2004, Uppala et al. 2005) for wind stress. See Table 4 for global averages and Fig. 5 for global statistics
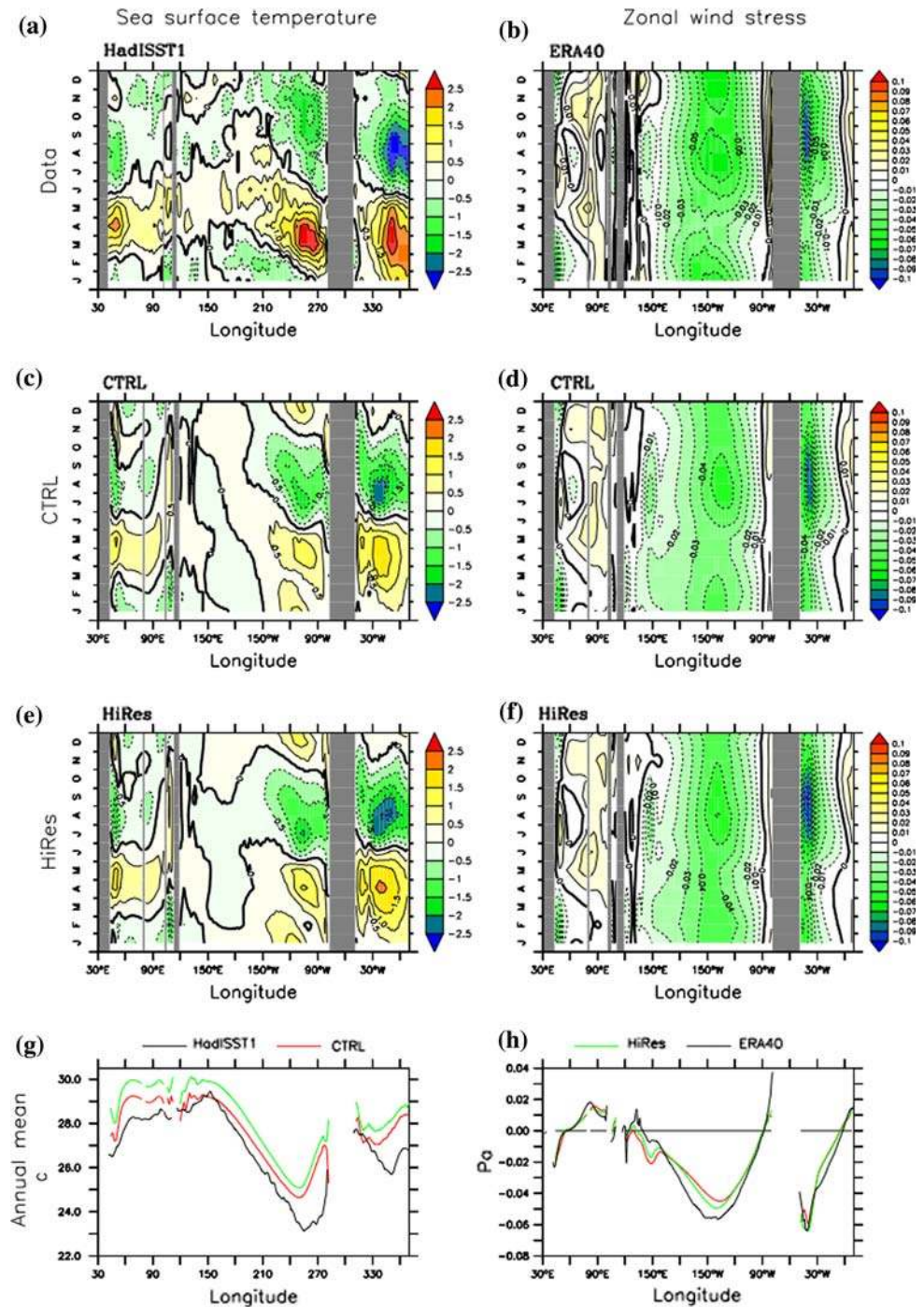
This can either be due atmosphere feedbacks (Philip and Van Oldenborgh 2006; Sun et al. 2006) or to ocean feedbacks (Fedorov 2007). Indeed, for instance, the surface heat flux damping associated with ENSO in Niño3 is only -5 W m^{-2} K^{-1} whereas it reached -20 W m^{-2} K^{-1} in ERA40. The ENSO frequency, as measured by the peak of the Niño3 SSTA spectra, is too high in CTRL (about 2.7 years vs. 4–5 years in observations, Guilyardi 2006).

In HiRes, the amplitude of the SST anomaly standard deviation is even larger than in CTRL (Fig. 18c) and reaches 1.2°C in Niño3. The zonal wind stress response is much improved compared to CTRL (Fig. 18f, g) even if it is still too weak. The coupling strength (Fig. 18i, 6.0×10^{-3} N m^{-2} K^{-1}) is consequently improved and, if we assume the damping feedbacks being the same (the atmosphere physical parameterisations of the two simulations
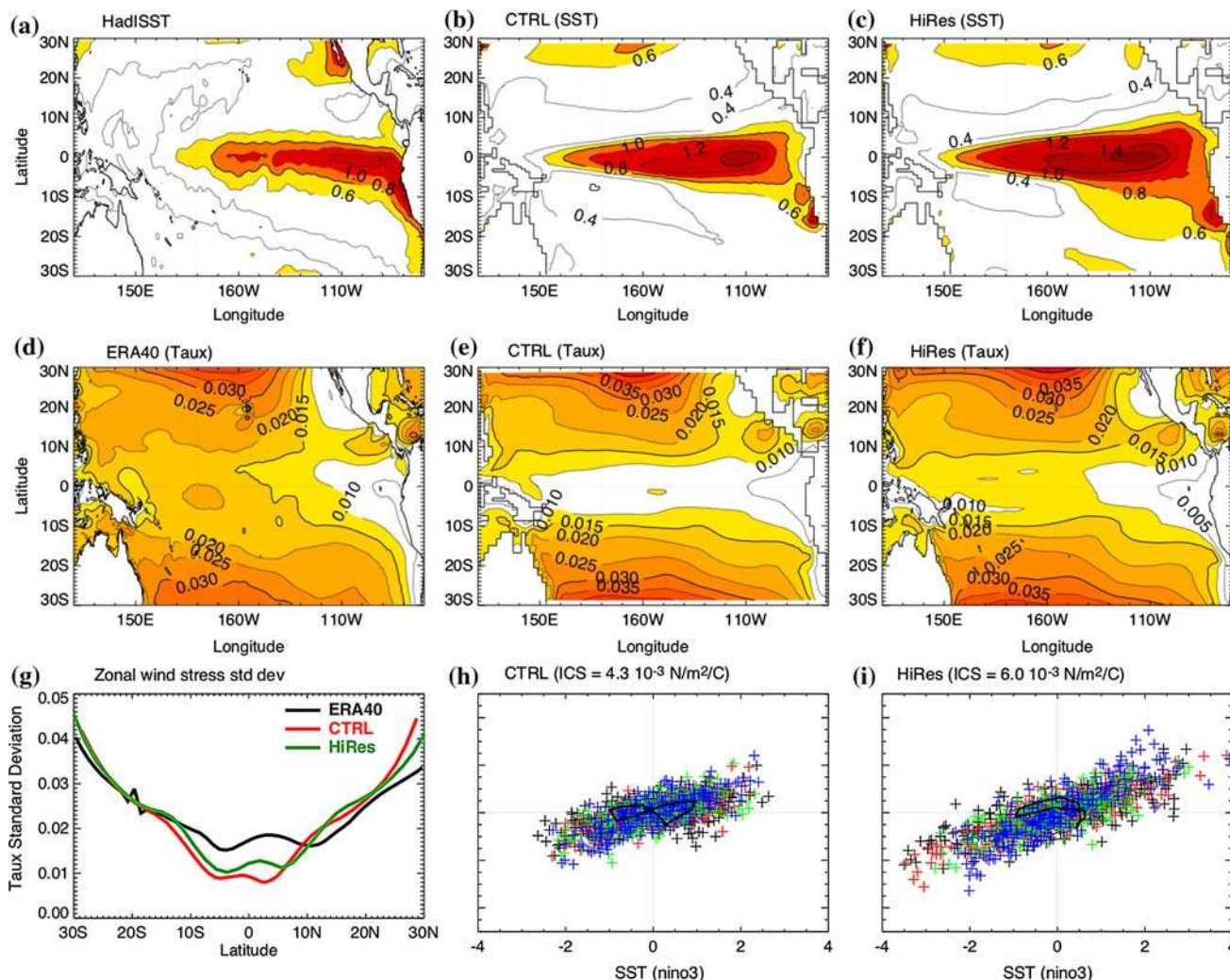
Fig. 18 Monthly standard deviation of SST and zonal wind stress for observations **a** HadISST (Rayner et al. 2003), **d** ERA40 (Uppala et al. 2005), **b** and **e** CTRL 100 years. **c** and **f** HiRes 100 years. **g** Zonal mean of wind stress standard deviation between 180 W and 140 W (*black* ERA40, *red* CTRL, *green* HiRes). **h**, **i** Interannual coupling strength for CTRL (**h**), linear fit $= 4.3 \times 10^{-3}$ N m^{-2} K^{-1}) and HiRes (**i**), linear fit $= 6.0 \times 10^{-3}$ N m^{-2} K^{-1}), measured as the slope of monthly anomaly of $\text{Tau}_{\text{Niño4}} = f(\text{anomaly of SST}_{\text{Niño3}})$. Contours are 0.2°C for (**a**–**c**) and 0.05 N m^{-2} for (**d**–**f**)

are the same and the heat flux feedback in Niño3 is also weak in HiRes at -6 W m^{-2} K^{-1}), this can explain the stronger ENSO amplitude via a stronger positive Bjerknes feedbacks. Three possible reasons can be put forward to explain the clear improvement of equatorial zonal wind stress variability in HiRes compared to CTRL (Fig. 18e–g). First the atmosphere has a better resolution and can then better respond to the ocean scale SST variability, confined in the 2°S/2°N wave guide. Second, the atmosphere has more degrees of freedom and scale interactions can transfer more energy from synoptic and intra-seasonal scales to interannual scales (Guilyardi et al. 2004, for similar results with the SINTEX model). And third, the atmosphere can better react to the tropical instability waves in the equatorial east Pacific ocean, which act as a momentum sink for the

atmosphere, thereby reduced the mean wind stress bias and allowing stronger interannual variability (Guilyardi 2006). The ENSO frequency in HiRes has now a 3.5 yrs peak in addition to the 2.7 years of CTRL (not shown). These improvements agree with other studies in which the atmosphere resolution was enhanced (Guilyardi et al. 2004; Navarra et al. 2008).

Both CTRL and HiRes large ENSO amplitude suggest that the damping processes are too weak in the model. These can be either due to atmosphere radiative feedbacks (Sun et al. 2006) or ocean dissipation (Fedorov 2007) and further work is needed to elucidate the origin of this bias. In any case, it seems that CTRL is getting the right ENSO amplitude for the wrong reasons, i.e. both too weak Bjerknes zonal wind/SST feedback and too weak damping.

The combined effect of this biases can also explain why the model cannot develop full blown large thermocline events and is therefore locked into a SST mode, favouring higher than observed ENSO frequency (2 year dominant peak, see Guilyardi 2006).

5 Conclusion

This manuscript describes the version 4 of the IPSL coupled ocean–atmosphere model. Specific care was put to have local and global conservation of heat and water fluxes. The heat flux budget confirms this closure, which allows long-term climate simulations, needed for studying processes of the present climate variability as well as paleoclimates.

The comparison of two versions of the coupled ocean–atmosphere model with two different atmospheric resolutions allows us to investigate the interactions and feedbacks between the atmospheric dynamics and the global and local climate. The control simulation corresponds to the IPSL reference sent to the WCRP/CMIP3 IPCC 2007 database (Meehl et al. 2007). It is compared with a simulation with higher resolution. The adjustment phases of the two resolutions are very similar, with the same characteristic timescale of adjustments. The global equilibrium is slightly different between the two versions. At higher resolution, the snow cover and the sea ice cover at high latitudes are reduced, with a lower albedo, inducing a warmer atmosphere. This warming propagates to the surface ocean, and penetrates in the ocean down to 2,000 m in the southern subtropics and in the high latitudes of both hemispheres.

In a first approximation, model biases are close to biases found in atmosphere alone simulations (Hourdin et al. 2006). The increase in resolution improves several aspect of the simulated climate in atmosphere alone and coupled simulations, like the storm-tracks, the characteristics of the North Atlantic oscillation and the seasonal and inter-annual variability in the tropics. On the contrary, the African monsoon remains poorly simulated at both resolutions.

The increase in atmospheric resolution improves the mid and high latitudes wind (mean state and variability). The better structure of surface winds strengthen the surface ocean circulation, transporting more salt towards the high latitudes of the Atlantic ocean, reducing the sea ice cover, and increasing the oceanic convection and the AMOC. However, the increase in gyre salt transport is not sufficient to set deep convection in the Labrador Sea, which is related to the excess of precipitation minus evaporation north of 40°N. This explains the remaining bias in the AMOC intensity, which is therefore certainly related to an excess of precipitation minus evaporation north of 40°N.

In the tropics the model performs reasonably well, for both seasonal and interannual variability. ENSO amplitude is about right in the control simulation, and becomes too large at higher resolution. The dynamical coupling strength between SST and wind anomalies is too weak in the control, and is strongly improved at higher resolution. The damping processes are too weak for both atmosphere resolutions, and further work is needed to elucidate why.

We conclude that the increase in horizontal resolution for the atmosphere in the climate model IPSL-CM4 leads to substantial improvements in atmospheric circulation, but also in thermohaline circulation and sea ice cover pattern. The choice of the atmospheric model resolution for the next IPCC report needs to be evaluated carefully in order to find the best compromise between representation of climate and computational costs. The present study actually shows that there may exist thresholds in atmospheric resolution that leads to large improvements for the climate system modelling. New simulations at higher atmospheric resolutions (144 × 144, 192 × 144, 192 × 192, etc.) will be considered.

Appendix 1: Interface for coupling the turbulent fluxes

A first standard interface for the coupling between the surface and the atmosphere was proposed by the PILPS project (Polcher et al. 1998, 2005). A drawback of the proposed approach is that the separation between the solving of the turbulent fluxes in the boundary layer and the solving of the temperature by the surface model is not complete. Indeed, the time evolution of the first atmospheric level variables (Polcher et al. 1998) is a function of the surface flux, but also of some surface coefficients. We overcome this difficulty by rewriting the discretized form of the vertical diffusion equation of the first atmospheric level and by considering explicitly the flux $F_{X,1/2}^{t+\delta t}$ between layer 1 and the surface:

$$\frac{X_1^t - X_1^{t+\delta t}}{\delta t} = \frac{1}{\delta z_1}\left(K_{X,3/2}\frac{X_2^{t+\delta t} - X_1^{t-\delta t}}{\delta z_{3/2}} - F_{X,1/2}^{t+\delta t}\right) \qquad (1)$$

and

$$F_{X,1/2}^{t+\delta t} = K_{X,1/2}\frac{X_1^{t+\delta t} - X_0^{t+\delta t}}{\delta z_{1/2}} \quad (2)$$

Variables X stands for the dry static energy, the specific humidity or the wind speed, $F_{X,k-1/2}$ is the flux of X at interface $k - 1/2$ (between level k and $k - 1$), $K_{X,k-1/2}$ is the vertical diffusion coefficient for variable X at this level; δz_k is the thickness of layer k and δz_{k+1} is the distance between the centres of layers k and $k - 1$.

1.1 In the boundary layer

To solve the vertical diffusion equation in the boundary layer, each variable of level k is written as a function of the variable of the level below $k - 1$, for all levels except level 1:

$$X_k^{t+\delta t} = A_{X,k}X_{X,k-1}^{t+\delta t} + B_{X,k} \text{ for } k \geq 2 \quad (3)$$

For level 1, $X_2^{t+\delta t}$ may be suppressed from Eq. 1, using:

$$A_{X,1} = -\frac{\delta t}{\delta z_1 C_{X,1}} \quad (4)$$

and

$$X_1^{t+\delta t} = A_{X,1}F_{X,1/2}^{t+\delta t} + B_{X,1} \quad (5)$$

$$A_{X,1} = -\frac{\delta t}{\delta z_1 C_{X,1}} \quad (6)$$

$$B_{X,1} = \left(X_1^t + \frac{\delta t K_{X,3/2}}{\delta z_1 \delta z_{3/2}}\right)\frac{1}{C_{X,1}} \quad (7)$$

and

$$C_{X,1} = 1 + \frac{\delta t K_{X,3/2}}{\delta z_1 \delta z_{3/2}}(1 - A_{X,2}) \quad (8)$$

One may verify that Eqs. 5–8 make only use of the flux with surface $F_{X,1/2}^{t+\delta t}$ and of atmospheric variables above layer 1. There is no use of surface variable or surface coefficient. For each variable X, variables $X_{X,1}$, $A_{X,1}$ and $B_{X,1}$ are transmitted by the boundary layer model to the surface model.

1.1.1 In the surface model

The surface model has to compute the surface flux $F_{X,1/2}^{t+\delta t}$ for each variable X. For the temperature and the humidity at the surface, the new values $X_1^{t+\delta t}$ are computed (if required) through the energy and water budget of the surface. The coupling between atmosphere and surface being implicit, a relationship between $F_{X,1/2}^{t+\delta t}$ and $X_0^{t+\delta t}$ is required. This is obtained by combining Eqs. 2–5:

$$F_{X,1/2}^{t+\delta t} = \frac{K_{X,1/2}}{\delta z_{1/2} - K_{X,1/2}A_{X,1}}\left(B_{X,1} - X_0^{t+\delta t}\right) \quad (9)$$

1.2 Decomposition of the oceanic heat transport

The oceanic heat transport across a latitude λ due to advection is computed as:

$$F = \int_{z=0}^{\text{bottom}} \int \rho C_p T v r_a \cos(\lambda) d\varphi dz \quad (10)$$

c mass, C_p the heat capacity per mass unit, T the temperature, v the northward velocity, r_a the Earth radius, φ the longitude and z the depth. T and z the depth. T, a and v are separated in $T = \overline{T} + T'$ and $v = \overline{v} + v'$, where the overline denotes the latitudinal average, and prime the latitudinal anomaly. The transport can be decomposed (2001) as:

$$F = \iint \rho C_p \overline{T}\,\overline{v} r_a \cos(\lambda) d\varphi dz$$
$$+ \iint \rho C_p T' v' r_a \cos(\lambda) d\varphi dz \quad (11)$$

The first term is the overturning transport and the second one the gyre transport.

1.3 Time filtering of snow accumulation on land ice

On land–ice surface, the local snow mass is limited to 3,000 kg m^{-2}. At each time-step, the snow mass over this limit $C(t)$ is computed. The calving C^* send to ocean is computed as a filtered snow mass $C(t) = (\Delta t/\tau)C(t) + (1 - \Delta t/\tau).C \times (t - 1)$, where Δt is the model time-step and τ is a characteristic time, set to 10 years in all experiments.

References

Alkama R, Kageyama M, Ramstein G (2006) Freshwater discharges in a simulation of the Last Glacial Maximum climate using improved river routing. Geophys Res Let 33(21)

Andrich P (1988) OPA—a multitasked ocean general circulation model—reference manual. LODYC, Université Paris VI, France, p 60

Ball JT, Woodrow TE, Berry JA (1987) A model predicting stomatal conductance and its contribution to the control of photosynthesis under different environmental conditions. Prog Photosynth 4:221–224

Barkstrom BR (1984) The Earth radiation budget experiment (ERBE). Bull Am Met Soc 65:1170–1185

Beckman A (1998) The representation of bottom boundary layer processes in numerical ocean circulation models. In: Chassignet EP, Verron J (eds) Ocean modeling and parametrization. Kluwer, Norwell

Boning CW, Holland WR, Bryan FO, Danabasoglu G, Mcwilliams JC (1995) An overlooked problem in model simulations of the thermohaline circulation and heat-transport in the Atlantic-Ocean. J Clim 8(3):515–523

Bony S, Emanuel KA (2001) A parameterization of the cloudiness associated with cumulus convection; evaluation using TOGA COARE data. J Atmos Sci 58(21):3,158–3,183

Bourke RH, McLaren AS (1992) Contour mapping of Arctic basin ice draft and roughness parameters. J Geophy Res-Oceans 97(C11):17715–17728

Braconnot P (1998) Tests de sensibilité avec le modèle d'atmosphère du LMD en vue d'améliorer le couplage avec l'océan, note technique IPSL 0076, IPSL, p 39

Braconnot P, Marti O (2003) Impact of precession on monsoon characteristics from coupled ocean atmosphere experiments: changes in Indian monsoon and Indian ocean climatology. Mar Geol 201(1–3):23–34

Braconnot P, Marti O, Joussaume S (1997) Adjustment and feedbacks in a global coupled ocean–atmosphere model. Clim Dyn 13(7–8):507–519

Braconnot P, Joussaume S, Marti O, de Noblet N (1999) Synergistic feedbacks from ocean and vegetation on the African monsoon response to mid-Holocene insolation. Geophys Res Lett 26(16):2481–2484

Braconnot P, Joussaume S, Marti O, de Noblet N (2000) Impact of ocean and vegetation feedback on 6 ka monsoon changes. Third PMIP Workshop, La Huardière, Canada, WCRP

Braconnot P, Hourdin F, Bony S, Dufresne J-L, Grandpeix J-Y, Marti O (2007a) Impact of different convective cloud schemes on the simulation of the tropical seasonal cycle in a coupled ocean–atmosphere model. Clim Dyn 29:501–520. doi:10.1007/s00382-007-0244-y

Braconnot P, Otto-Bliesner B, Harrison S, Joussaume S, Peterchmitt JY, Abe-Ouchi A, Crucifix M, Driesschaert E, Fichefet T, Hewitt CD, Kageyama M, Kitoh A, Laine A, Loutre MF, Marti O, Merkel U, Ramstein G, Valdes P, Weber SL, Yu Y, Zhao Y (2007b) Results of PMIP2 coupled simulations of the Mid-Holocene and last glacial maximum. Part 1. Experiments and large-scale features. Clim Past 3(2):261–277

Bryden HL, Imawaki S (2001) Ocean heat transport. In: Siedler G, Church JA, Gould J (eds) Ocean circulation and climate: observing and modelling the global ocean. Academic Press, San Diego, pp 445–474

Collatz GJ, Ribas-Carbo M, Berry JA (1992) Coupled photosynthesis-stomatal conductance model for leaves of C4 plants. Aust J Plant Physiol 19(5):519–538

Cunningham SA, Alderson SG, King BA, Brandon MA (2003) Transport and variability of the Antarctic circumpolar current in drake passage. J Geophys Res-Oceans 108(C5). doi:10.1029/2001JC001147

de Boyer Montégut CD, Madec G, Fischer AS, Lazar A, Iudicone D (2004) Mixed layer depth over the global ocean: an examination of profile data and a profile-based climatology. J Geophys Res-Oceans 109(C12). doi:10.1029/2004JC002378

DeWeaver E, Bitz CM (2006) Atmospheric circulation and its effect on Arctic sea ice in CCSM3 simulations at medium and high resolution. J Clim 19(11):2415–2436

Dong BW, Valdes PJ (2000) Climates at the last glacial maximum: Influence of model horizontal resolution. J Clim 13(9):1554–1573

Ducoudré N, Laval K, Perrier A (1993) SECHIBA, a new set of parameterizations of the hydrologic exchanges at the land–atmosphere interface within the LMD atmospheric general circulation model. J Clim 6:248–273

Dufresne J-L, Grandpeix J-Y (1996), Raccordement des modèles thermodynamiques de glace, d'océan et d'atmosphère, Note Interne 205, Laboratoire de Métérologie Dynamique

Dufresne JL, Friedlingstein P, Berthelot M, Bopp L, Ciais P, Fairhead L, Le Treut H, Monfray P (2002) On the magnitude of positive feedback between future climate change and the carbon cycle. Geophys Res Lett 29(10). doi:10.1029/2001GL013777

Dufresne JL, Quaas J, Boucher O, Denvil S, Fairhead L (2005) Contrasts in the effects on climate of anthropogenic sulfate aerosols between the 20th and the 21st century. Geophys Res Lett 32(21). doi:10.1029/2005GL023619

Eichelberger SJ, Hartmann DL (2007) Zonal jet structure and the leading mode of variability. J Clim 20(20):5149–5163

Emanuel KA (1991) The theory of Hurricanes. Ann Rev Fluid Mech 23:179–196

Farquhar GD, Caemmerer SV, Berry JA (1980) A biochemical-model of photosynthetic CO_2 assimilation in leaves of C-3 species. Planta 149(1):78–90

Fedorov AV (2007) Net energy dissipation rates in the tropical ocean and ENSO dynamics. J Clim 20(6):1108–1117

Fichefet T, Morales-Maqueda AM (1997) Sensitivity of a global sea ice model to the treatment of ice thermodynamics and dynamics. J Geophys Res 102(6):12609–12646

Fichefet T, Morales-Maqueda AM (1999) Modelling the influence of snow accumulation and snow–ice formation on the seasonal cycle of the Antarctic sea–ice cover. Clim Dyn 15(4):251–268

Filiberti M-A, Dufresne J-L, Grandpeix J-Y (2001) Reference manual for IGLOO sea ice model. Note technique du Pôle de modélisation, Institut Pierre-Simon Laplace, 35 pp

Fouquart Y, Bonnel B (1980) Computations of solar heating of the Earth's atmosphere: a new parametrization. Contrib Atmos Phys 53:35–62

Friedlingstein P, Bopp L, Ciais P, Dufresne JL, Fairhead L, LeTreut H, Monfray P, Orr J (2001) Positive feedback between future climate change and the carbon cycle. Geophys Res Lett 28(8):1543–1546

Ganachaud A, Wunsch C (2000) Improved estimates of global ocean circulation, heat transport and mixing from hydrographic data. Nature 408(23 November):453–457

Ganachaud A, Wunsch C (2003) Large-scale ocean heat and freshwater transport during the World ocean circulation experiment. J Clim 16:696–705

Gloersen P, Campbell WJ (1991) Recent variations in Arctic and Antarctic sea–ice covers. Nature 352:33–36

Guilyardi E (2006) El Niño-mean state-seasonal cycle interactions in a multi-model ensemble. Clim Dyn 26(4):329–348

Guilyardi E, Madec G, Terray L (2001) The role of lateral ocean physics in the upper ocean thermal balance of a coupled ocean–atmosphere GCM. Clim Dyn 17(8):589–599

Guilyardi E, Gualdi S, Slingo JM, Navarra A, Delecluse P, Cole J, Madec G, Roberts M, Latif M, Terray L (2004) Representing El Niño in coupled ocean–atmosphere GCMs: the dominant role of the atmospheric component. J Clim 17(24):4623–4629

Hack JJ, Caron JM, Danabasoglu G, Oleson KW, Bitz C, Truesdale JE (2006a) CCSM-CAM3 climate simulation sensitivity to changes in horizontal resolution. J Clim 19(11):2267–2289

Hack JJ, Caron JM, Yeager SG, Oleson KW, Holland MM, Truesdale JE, Rasch PJ (2006b) Simulation of the global hydrological cycle in the CCSM community atmosphere model version 3 (CAM3): mean features. J Clim 19(11):2199–2221

Hagemann S, Dumenil L (1998) A parametrization of the lateral waterflow for the global scale. Clim Dyn 14(1):17–31

Hibler WDI (1979) A dynamic thermodynamic sea ice model. J Phys Oceanogr 9:815–846

Hoskins BJ, Hodges KI (2002) New perspectives on the Northern Hemisphere winter storm tracks. J Atmos Sci 59(6):1041–1061

Hourdin F, Issartel JP, Cabrit B, Idelkadi A (1999) Reciprocity of atmospheric transport of trace species. Comptes Rendus de L'Académie des Sciences, Serie II, Fascicule a, Sciences de la Terre et des Planètes 329(9):623–628

Hourdin F, Musat I, Bony S, Braconnot P, Codron F, Dufresne JL, Fairhead L, Filiberti MA, Friedlingstein P, Grandpeix JY, Krinner G, Levan P, Li ZX, Lott F (2006) The LMDZ4 general

circulation model: climate performance and sensitivity to parametrized physics with emphasis on tropical convection. Clim Dyn 27(7–8):787–813

IPCC (2007) Climate change 2007—the physical science basis, contribution of working group I to the fourth assessment report of the IPCC. IPCC, Geneva, 981 pp

Jakobsson M, Cherkis NZ, Woodward J, Macnab R, Coakley B (2000) New grid of Arctic bathymetry aids scientists and mapmakers. EOS Trans 81(9):89, 93, 96

Jones PW (1999) First- and second-order conservative remapping schemes for grid in spherical coordinates. Mont Weath Rev 127(9):2204–2210

Kageyama M, Valdes PJ, Ramstein G, Hewitt C, Wyputta U (1999) Northern hemisphere storm tracks in present day and last glacial maximum climate simulations: a comparison of the European PMIP models. J Clim 12(3):742–760

Kageyama M, Peyron O, Pinot S, Tarasov P, Guiot J, Joussaume S, Ramstein G (2001) The last glacial maximum climate over Europe and western Siberia: a PMIP comparison between models and data. Clim Dyn 17(1):23–43

Kalnay E, Kanamitsu M, Kistler R, Collins W, Deaven D, Gandin L, Iredell M, Saha S, White G, Woollen J, Zhu Y, Chelliah M, Ebisuzaki W, Higgins W, Janowiak J, Mo KC, Ropelewski C, Wang J, Leetmaa A, Reynolds R, Jenne R, Joseph D (1996) The NCEP/NCAR 40-year reanalysis project. Bull Am Met Soc 77(3):437–471

Khodri M, Cane MA, Kukla G, Gavin J, Braconnot P (2005) The impact of precession changes on the Arctic climate during the last interglacial–glacial transition. Earth Planet Sci Lett 236(1–2):285–304

Krinner G, Genthon C, Li Z-X, Le Van P (1997) Studies of the Antarctic climate with a stretched-grid general circulation model. J Geophys Res 102:13731–13745

Krinner G, Viovy N, de Noblet-Ducoudré N, Ogée J, Polcher J, Friedlingstein P, Ciais P, Sitch S, Prentice IC (2005) A dynamic global vegetation model for studies of the coupled atmosphere–biosphere system. Glob Biogeochem Cycle 19(1). doi:10.1029/2003GB002199

L'Heveder B (1999) Variabilité saisonnière et interannuelle des glaces de mer en Arctique: influence des interactions avec l'atmosphère. Ph.D., Paris VI, pp 132

Le Clainche Y (1996) Modélisation du ruissellement dans un modèle couplé, Tech. rep., LSCE, Saclay

Le Treut H, Li Z-X (1991) Sensitivity of an atmospheric general circulation model to prescribed SST changes: feedback effect associated with the simulation of the cloud optical properties. Clim Dyn 5:175–187

Levitus S (1982) Climatological atlas of the world ocean, 13. NOAA/ERL GFDL, Washington, p 173

Lott F (1997) The transient emission of propagating gravity waves by a stably stratified shear layer. Quart J Roy Met Soc 123(542):1603–1619

Lott F (1999) Alleviation of stationary biases in a GCM through a mountain drag parameterization scheme and a simple representation of mountain lift forces. Mont Weath Rev 127(5):788–801

Lythe MB, Vaughan DG (2001) BEDMAP: a new ice thickness and subglacial topographic model of Antarctica. J Geophys Res–Solid Earth 106:11335–11351

MacDonald A (1998) The global ocean: a hydrographic estimate and regional analysis. Prog Oceanogr 41:281–382

Madec G, Imbard M (1996) A global ocean mesh to overcome the North Pole singularity. Clim Dyn 12(6):381–388

Madec G, Delecluse P, Imbard M, Levy C (1997) OPA version 8.1 Ocean general circulation model reference manual, 3. LODYC, Technical Report, 91 pp

Marti O, Braconnot P, Bellier J, Benshila R, Bony S, Brockmann P, Cadule P, Caubel A, Denvil S, Dufresne JL, Fairhead L, Filiberti M-A, Foujols M-A, Fichefet T, Friedlingstein P, Goosse H, Grandpeix JY, Hourdin F, Krinner G, Lévy C, Madec G, Musat I, de Noblet N, Polcher J, Talandier C (2005) The new IPSL climate system model: IPSL-CM4, Note du Pôle de Modélisation 26. Institut Pierre Simon Laplace, Paris, p 84

Meehl GA, Covey C, Delworth TL, Latif M, McAvaney B, Mitchell JFB, Stouffer RJ, Taylor KE (2007) The WCRP CMIP3 multimodel dataset: a new era in climate change research. Bull Am Met Soc 88(9):1383–1394. doi:10.1175/BAMS-88-9-1383

Morcrette JJ, Smith L, Fouquart Y (1986) Pressure and temperature dependence of the absorption in longwave radiation parametrizations. Contrib Atmos Phys 59(4):455–469

Murray RJ (1996) Explicit generation of orthogonal grids for ocean models. J Comput Phys 126:251–273

Navarra A, Gualdi S, Masina S, Behera S, Luo JJ, Masson S, Guilyardi E, Delecluse P, Yamagata T (2008) Atmospheric horizontal resolution affects tropical climate variability in coupled models. J Clim 21(4):730–750

Ngo-Duc T, Polcher J, Laval K (2005) A 53-year forcing data set for land surface models. J Geophys Res (Atm) 110(D6). doi:10.1029/2004JD005434

Philip S, Van Oldenborgh GJ (2006) Shifts in ENSO coupling processes under global warming. Geophys Res Let 33(11). doi:10.1029/2006GL026196

Pinot S, Ramstein G, Harrison SP, Prentice IC, Guiot J, Stute M, Joussaume S (1999) Tropical paleoclimates at the last glacial maximum: comparison of paleoclimate modeling intercomparison project (PMIP) simulations and paleodata. Clim Dyn 15(11):857–874

Polcher J, McAvaney B, Viterbo P, Gaertner MA, Hahmann A, Mahfouf JF, Noilhan J, Phillips T, Pitman A, Schlosser CA, Schulz JP, Timbal B, Verseghy D, Xue Y (1998) A proposal for a general interface between land surface schemes and general circulation models. Glob Planet Change 19(1–4):261–276

Quadrelli R, Wallace JM (2004) A simplified linear framework for interpreting patterns of Northern Hemisphere wintertime climate variability. J Clim 17(19):3728–3744

Rayner NA, Parker DE, Horton EB, Folland CK, Alexander LV, Rowell DP, Kent EC, Kaplan A (2003) Global analyses of sea surface temperature, sea ice, and night marine air temperature since the late nineteenth century. J Geophys Res-Atmospheres 108(D14). doi:10.1029/2002JD002670

Reynolds RW (1988) A real time global sea-surface temperature analysis. J Clim 1:75–86

Roullet G, Madec G (2000) Salt conservation, free surface, and varying levels: a new formulation for ocean general circulation models. J Geophys Res (Oceans) 105(10):23927–23942

Russell J, Stouffer RJ, Dixon KW (2006) Intercomparison of the Southern Ocean circulations in IPCC coupled control simulations. J Clim 19:4560–4575

Sadourny R, Laval K (1984) January and July performance of the LMD general circulation model. New perspectives in climate modelling, developments in atmospheric science. In: Berger AL, Nicolis C (eds). 16:173–198

Smith WHF, Sandwell DT (1997) Global sea-floor topography from satellite altimetry and ship depth souding. Science 277:1952–1956

Steele M, Morley R, Ermold W (2001) PHC: a global ocean hydrography with a high-quality Arctic Ocean. J Clim 14(9):2079–2087

Stommel H (1961) Thermohaline convection with 2 stable regimes of flow. Tellus 13(2):224–230

Sun DZ, Zhang T, Covey C, Klein SA, Collins WD, Hack JJ, Kiehl JT, Meehl GA, Held IM, Suarez M (2006) Radiative and dynamical

feedbacks over the equatorial cold tongue: results from nine atmospheric GCMs. J Clim 19(16):4059–4074

Swingedouw D, Braconnot P, Marti O (2006) Sensitivity of the Atlantic meridional overturning circulation to the melting from northern glaciers in climate change experiments. Geophys Res Lett 33(7). doi:10.1029/2006GL025765

Swingedouw D, Braconnot P, Delecluse P, Guilyardi E, Marti O (2007) The impact of global freshwater forcing on the thermohaline circulation: adjustment of North Atlantic convection sites in a CGCM. Clim Dyn 28(2–3):291–305

Talley LD, Reid JL, Robbins PE (2003) Data-based meridional overturning streamfunctions for the global ocean. J Clim 16(19):3213–3226

Taylor KE (2001) Summarizing multiple aspects of model performance in a single diagram. J Geophys Res-Atmospheres 106(D7):7183–7192

Tiedtke M (1989) A comprehensive mass flux scheme for cumulus parameterization in large-scale models. Mont Weath Rev 117:1179–1800

Timmermann R, Goosse H, Madec G, Fichefet T, Ethé C, Dulière V (2004) On the representation of high latitude processes in the ORCA-LIM global coupled sea ice–ocean model. Ocean Mod 8(1–2):175–201

Trenberth KE, Caron JM (2001) Estimates of meridional atmosphere and ocean heat transports. J Clim 14(16):3433–3443

Uppala SM, Kallberg PW, Simmons AJ, Andrae U, Bechtold VD, Fiorino M, Gibson JK, Haseler J, Hernandez A, Kelly GA, Li X, Onogi K, Saarinen S, Sokka N, Allan RP, Andersson E, Arpe K, Balmaseda MA, Beljaars ACM, Van De Berg L, Bidlot J, Bormann N, Caires S, Chevallier F, Dethof A, Dragosavac M, Fisher M, Fuentes M, Hagemann S, Holm E, Hoskins BJ, Isaksen L, Janssen PAEM, Jenne R, McNally AP, Mahfouf JF, Morcrette JJ, Rayner NA, Saunders RW, Simon P, Sterl A, Trenberth KE, Untch A, Vasiljevic D, Viterbo P, Woollen J (2005) The ERA-40 re-analysis. Quart J Roy Met Soc 131(612):2961–3012

Valcke S (2006), OASIS3 user guide (prism_2-5), PRISM support initiative 3, 68 pp

Van Leer B (1977) Towards the ultimate conservative difference scheme: IV a new approach to numerical convection. J Comput Phys 23:276–299

Verant S, Laval K, Polcher J, De Castro M (2004) Sensitivity of the continental hydrological cycle to the spatial resolution over the Iberian Peninsula. J Hydrometeorol 5(2):267–285

Wijffels SE, Schmitt RW, Bryden HL, Stigebrandt A (1992) Transport of fresh-water by the Oceans. J Phys Oceanogr 22(2):155–162

Wunsch C (2005) The total meridional heat flux and its oceanic and atmospheric partition. J Clim 18(21):4374–4380

Xie PP, Arkin PA (1997) Global precipitation: a 17-year monthly analysis based on gauge observations, satellite estimates, and numerical model outputs. Bull Am Met Soc 78(11):2539–2558